Importance of forearc topography for the triggering of aftershocks of megathrust earthquakes: Insights from mechanical models and the Tohoku-Oki and Maule earthquakes

Armin Dielforder[1], Gian Maria Bocchini[2], Andrea Hampel[1]

[1]Institut für Erdsystemwissenschaften, Abteilung Geologie, Leibniz Universität Hannover, Hannover, 30167, Germany
[2]Institut für Geologie, Mineralogie und Geophysik, Ruhr-Universität Bochum, Bochum, 44801, Germany

Correspondence to: Armin Dielforder (dielforder@geowi.uni-hannover.de)

Abstract. Aftershocks of megathrust earthquakes at subduction zones may be driven by stress arising from the topography of the forearc. However, the effect of topographic stress on aftershock triggering is quantitatively not well understood and has been neglected in Coulomb failure stress models that assess whether the stress change caused by an earthquake promotes or inhibits failure on nearby faults. Here we use analytical and numerical models to examine the importance of topographic stress on Coulomb failure stress changes caused by megathrust earthquakes. We show that topographic stress is a prerequisite for widespread aftershock seismicity in the forearc and that its superposition with tectonic stress leads to a dependence of the forearc stability on the stress state before and after the earthquake. The dependence can be taken into account by determining the Coulomb failure stress change between optimal failure planes before and after the earthquake, which requires constraining the total stresses in the forearc. Applying our modelling approach to the 2011 M_w 9.0 Tohoku-Oki and 2010 M_w 8.8 Maule megathrust earthquakes yields coseismic Coulomb failure stress changes of up to ~40 MPa, which promoted the majority of the aftershocks in the Japanese and Chilean forearcs. The model results further reveal that the spatial distribution of aftershocks was not only influenced by the megathrust stress drop and the proximity of faults to failure but also by local differences in forearc topography and pre-earthquake stress state. Our analysis highlights the significance of total stresses in Coulomb failure stress calculations, enabling a better estimation of seismic hazard at subduction zones.

1 Introduction

The concept of Coulomb failure stress change finds broad application to investigate earthquake-induced stress changes and the triggering of aftershocks in various tectonic settings including continental interiors and active margins (e.g., Bagge et al., 2018; Farías et al., 2011; King et al., 1994; Lin and Stein, 2004; Oppenheimer et al., 1988; Pace et al., 2014; Ryder et al., 2012; Saltogianni et al., 2021; Stein, 1999; Terakawa et al., 2013; Toda et al., 2011a). The Coulomb failure stress change (ΔCFS) describes the relative change in shear and normal stresses imparted by an earthquake on nearby faults and indicates whether it promotes (positive ΔCFS) or inhibits (negative ΔCFS) failure (e.g., King et al., 1994; Harris, 1998).

30 Over the past decades, the development of Coulomb failure stress models addressed various factors, including the effects of the tectonic regime and regional stress field on Coulomb failure stress changes, as well as the mechanisms influencing stress changes in the postseismic and interseismic periods, such as viscoelastic relaxation, poroelasticity and pore pressure changes (e.g., Bagge and Hampel., 2016; 2017; Cocco and Rice, 2002; Freed and Lin, 1998; Hainzl, 2004; Hardebeck, 2014; Hardebeck et al., 1998; Peikert et al., 2024; Peña et al., 2022; Segou and Parsons, 2020). One aspect that has found no

35 consideration in Coulomb failure stress models is the dependence of the regional stress field on topographic and tectonic stresses. It is the purpose of the present paper to show how the superposition of topographic and tectonic stresses at active margins influences the Coulomb failure stress change caused by megathrust earthquakes in the forearc.
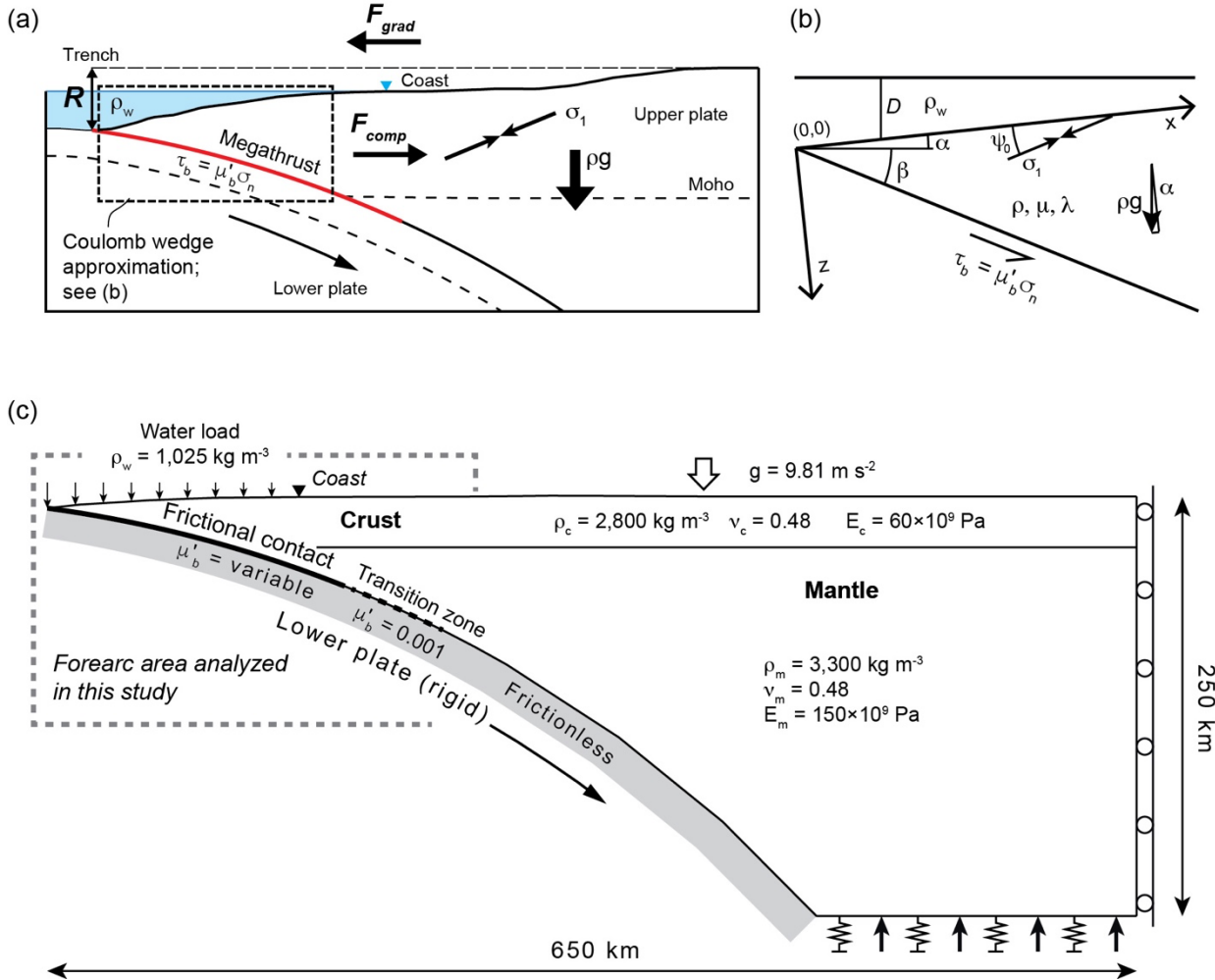
Topographic stress results from the gradient in potential energy that arises in the gravitational field of the Earth between areas of lower and higher elevation (e.g., Molnar and Lyon-Caen, 1988). Topographic stress is particularly relevant at active

40 continental margins, where the gradient in potential energy imposed by the continental margin relief, i.e., the difference in elevation between the oceanic trench and the mountains and volcanoes in the upper plate, induces margin-normal tension in the forearc (e.g., Lamb, 2006; Wang and He, 1999). The margin-normal tension is counteracted by the shear stress on the megathrust, which causes margin-normal compression (Fig. 1a). To a first approximation, the superposition of margin-normal tension and margin-normal compression determines the stress field in the forearc. During subduction earthquakes,

45 the shear stress on the megathrust decreases, which reduces the compression of the forearc and alters the superposition of stresses (e.g., Dielforder et al., 2023; 2020; Herman and Govers, 2020; Wang et al., 2019; Wang and Hu, 2006).

The decrease in megathrust shear stress (stress drop) and resulting stress changes may trigger aftershock seismicity in the forearc, as indicated by upper-plate normal faulting sequences after large megathrust earthquakes (e.g., Asano et al., 2011; Dewey et al., 2007; Farías et al., 2011; Hardebeck et al., 2012, Hasegawa et al., 2012; Ryder et al., 2012; Yoshida et al.,

50 2012). Normal faulting after the 2011 M_w 9.0 Tohoku-Oki earthquake, Japan, occurred in forearc areas that failed by thrust faulting before the earthquake (e.g., Hasegawa et al., 2012; Yoshida et al., 2012). The change in fault kinematics indicates that the Tohoku-Oki earthquake locally reversed the stress state in the forearc, which has been mechanically explained by the stress changes resulting from the stress drop on the megathrust (e.g., Cubas et al., 2013; Dielforder et al., 2023; Wang et al., 2019).

55 The details of stress changes caused by megathrust earthquakes and their potential to trigger aftershocks are, however, still not fully understood. In particular, assessing total stresses and stress changes at subduction zones requires accounting for the superposition of topographic and tectonic stresses and hence to include gravity, forearc topography and megathrust shear stresses in models. The parameters are not included in common Coulomb failure stress models based on dislocation solutions for a fault embedded in an elastic half-space (e.g., King et al., 1994; Lin and Stein, 2004). We therefore use in this study

60 mechanical models that allow calculating total stresses in consideration of gravity, forearc topography, and megathrust shear stress. We first use analytical stress solutions of the dynamic Coulomb wedge theory (Wang and Hu, 2006) to describe the main effects of topographic and tectonic stresses on Coulomb failure stress changes in a uniform subduction zone prism representing the frontal part of a forearc (Fig. 1b). We then use plane-strain finite-element models (Fig. 1c) to investigate

2

Coulomb failure stress changes caused by the 2011 M_w 9.0 Tohoku-Oki and the 2010 M_w 8.8 Maule earthquakes in the Japanese and Chilean forearcs, respectively. The finite-element models allow to investigate the stress changes in consideration of a more complex upper-plate structure and earthquake stress change.

Our analysis uses a two-dimensional simplification of a three-dimensional system, i.e., we investigate stresses in the vertical plane of cross section normal to the plate margin and do not address aspects of oblique plate convergence. We further assume in the finite-element models a linear-elastic rheology for the forearc and restrict our analysis to the immediate coseismic stress change induced by the earthquake. In the following, we use the rock mechanics convention of defining compressive stresses as positive.

2 Coulomb failure stress changes in an idealized Coulomb wedge

2.1 Application and implications of the dynamic Coulomb wedge theory

The dynamic Coulomb wedge theory describes the first order mechanics of subduction zone prisms in megathrust earthquake cycles by considering temporal variations in megathrust shear stress (Wang and Hu, 2006). The theory builds on the classical critical taper model (Dahlen, 1984; Zhao et al., 1986) and approximates the outermost part of the forearc as a uniform wedge of density ρ overlying the megathrust (Fig. 1b). The wedge geometry is defined by the surface slope angle α and basal dip angle β. The wedge has an elastic-perfectly Coulomb plastic rheology, i.e., it can be in a stable elastic state and in critical state at Coulomb failure. The Coulomb-plastic rheology is defined by the coefficient of friction μ and pore fluid pressure ratio

$$\lambda = (P - \rho_w gD)/(\sigma_z - \rho_w gD) \tag{1}$$

where *P* is pore fluid pressure within the wedge, ρ_w is water density, *D* is water depth, σ_z is stress in z-direction (see Fig. 1b for local coordinates) and *g* is gravitational acceleration (Dahlen, 1984, Wang and Hu, 2006). The megathrust shear stress can be written in terms of effective normal stress $\overline{\sigma}_n = \sigma_n(1 - \lambda)$ as

$$\tau_b = \frac{\mu'_b \overline{\sigma}_n}{(1-\lambda)} = \mu'_b \sigma_n \tag{2}$$

where μ'_b is the effective coefficient of megathrust friction and depends on both the intrinsic friction coefficient μ_b and the effect of pore fluid pressure ratio λ_b in the fault zone, i.e., $\mu'_b = \mu_b(1 - \lambda_b)$. For this study, it suffices to consider only values of μ'_b without defining μ_b and λ_b separately. Note that parameter μ'_b was termed μ''_b in Wang and Hu (2006) and that Dahlen (1984) and Wang and Hu (2006) used the term "effective coefficient of friction" to refer to parameter $\mu'_b/(1 - \lambda)$ instead of μ'_b as is common in Earth Science (cf. Hu and Wang, 2008; Wang et al., 2019).

The pore fluid pressure ratio in the wedge and the effective coefficient of megathrust friction determine the mechanical state of an elastic-perfectly Coulomb plastic wedge as qualitatively illustrated in Fig. 2a. The wedge may be in a critical state and fail by thrust faulting and normal faulting if μ'_b is sufficiently high and low, respectively,. For intermediate values of μ'_b, the wedge may be in a stable state, where the range of stability decreases with increasing λ. The stable state can be further distinguished into a compressively stable state in which the wedge experiences deviatoric compression, a neutrally stable

state (dashed horizontal line in Fig. 2a), and an extensionally stable state in which the wedge experiences deviatoric tension. The possible mechanical states are illustrated in Fig. 2c. Note that for high values of λ and low values of μ'_b, the wedge may attain a critical state at which both thrust faulting and normal faulting can occur (dashed part of the failure the envelope in Fig. 2a).
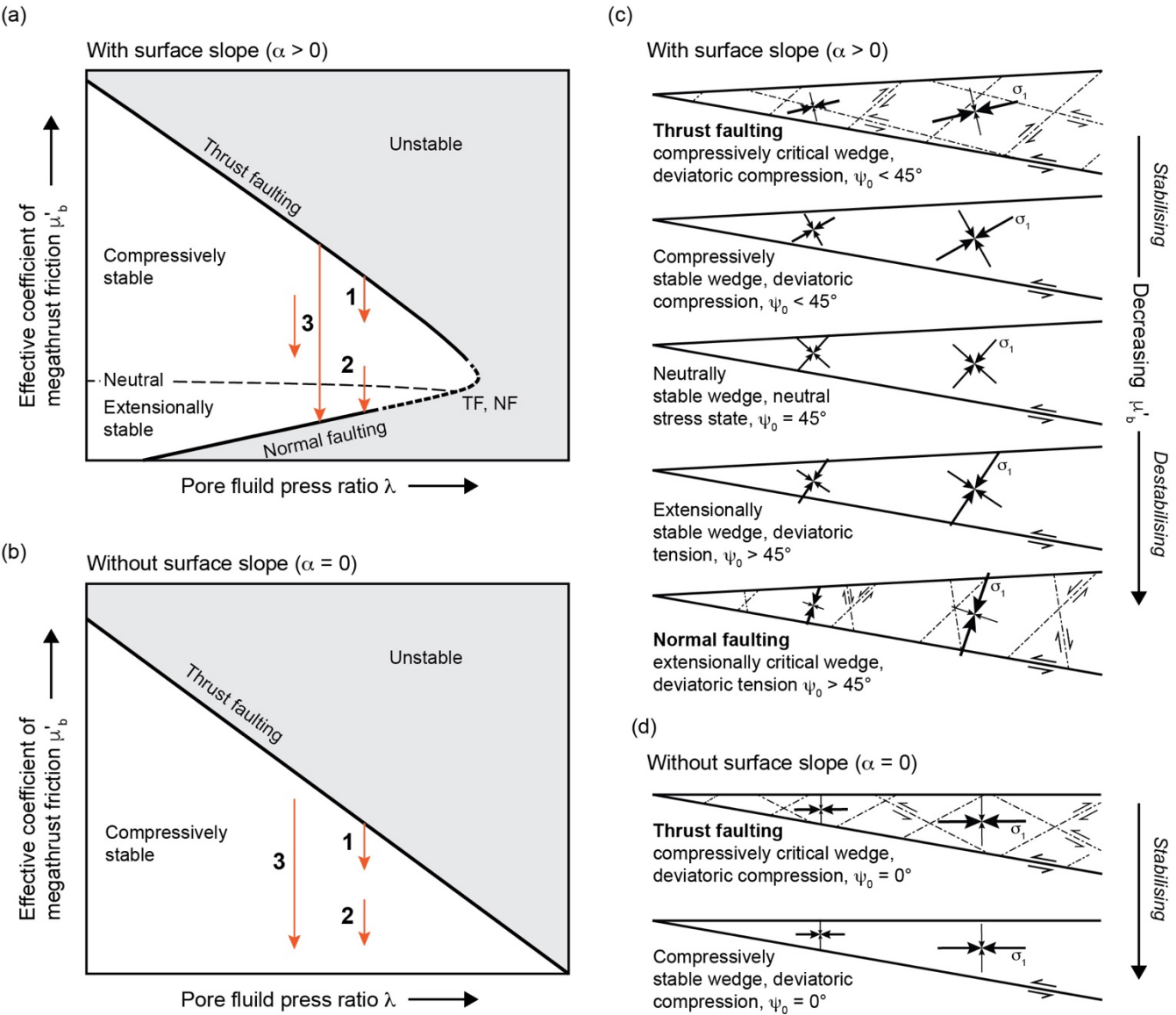
The λ–μ'_b space allows to investigate the mechanical states a wedge may achieve at different stages of an earthquake cycle (Wang and Hu, 2006). Over the interseismic period, the shear stress on the seismogenic megathrust increases progressively such that the maximum compression of the wedge occurs toward the end of the earthquake cycle. During megathrust earthquakes, the shear stress on the plate interface decreases abruptly due to coseismic weakening processes (e.g., Kanamori and Brodsky, 2004; Scholz 1998; Wang and Hu, 2006). The average stress drop on the megathrust can be modelled as a change in the effective coefficient of megathrust friction $\Delta\mu'_b = \mu'_{b\text{-pre}} - \mu'_{b\text{-post}}$, where $\mu'_{b\text{-pre}}$ and $\mu'_{b\text{-post}}$ are the μ'_b values that describe the megathrust shear stress just before and after the earthquake, respectively (Wang and Hu, 2006).

The effect of the stress drop on the mechanical stability of the wedge is illustrated for different scenarios in the λ–μ'_b space (Fig. 2a) by orange arrows. In the first scenario (1 in Fig. 2a), the wedge is in a compressively critical state and fails by thrust faulting before the earthquake, and in a compressively stable state after the earthquake. The stress drop on the megathrust stabilises the wedge. In the second scenario, the stress drop pushes the wedge from a compressively stable state into an extensionally critical state causing normal faulting. The stress drop destabilises the wedge, although the relative change in μ'_b is the same as in scenario 1; only the value of $\mu'_{b\text{-pre}}$ differs. Scenario 3 shows a stress drop that has no effect on the wedge stability. The large stress drop (larger arrow) pushes the wedge from a compressively critical state into a an extensionally critical state. The wedge is just as close to failure after the earthquake as it was before the earthquake. The same applies for the smaller stress drop, with the only difference that the wedge is compressively stable before and after the earthquake and not critical.

The above scenarios only apply if the surface slope angle $\alpha > 0$; i.e., the described effect of the stress drop on the wedge stability depends on topographic stress resulting from the gradient in potential energy. When $\alpha = 0$, there is no gradient in potential energy and the Coulomb wedge can only attain a compressively critical state and fail by thrust faulting or a compressively stable state. In that case, the megathrust stress drop always stabilizes the wedge (scenarios 1-3 in Fig. 2c, d)

2.2 Total stress and Coulomb failure stress changes in a Coulomb wedge

The tendency of a megathrust stress drop to stabilise or destabilise the Coulomb wedge does not depend on whether or not the wedge attains a critical state and can be described in terms of Coulomb failure stresses without determining λ. For this,

we start by considering the total stresses in a Coulomb wedge. The analysis is based on the analytical expressions of the dynamic Coulomb wedge theory summarised in Appendix 1.

150 Fig. 3a illustrates the stress in a Coulomb wedge as function of μ'_b in terms of stresses σ_x and σ_z. The stress solutions are obtained for a non-cohesive, stable reference wedge model with $\alpha = 3°$, $\beta = 10°$, $\mu = 0.7$, and $\lambda = 0$. The dependence of stress on μ'_b is everywhere the same in the uniform wedge (Dahlen, 1984, Wang and Hu, 2006) and is described in terms of normalized stress values. To allow an estimation of total stresses, we provide stress values at 10 km depth in the wedge on the secondary ordinate (right vertical axis) in Fig. 3a.

155
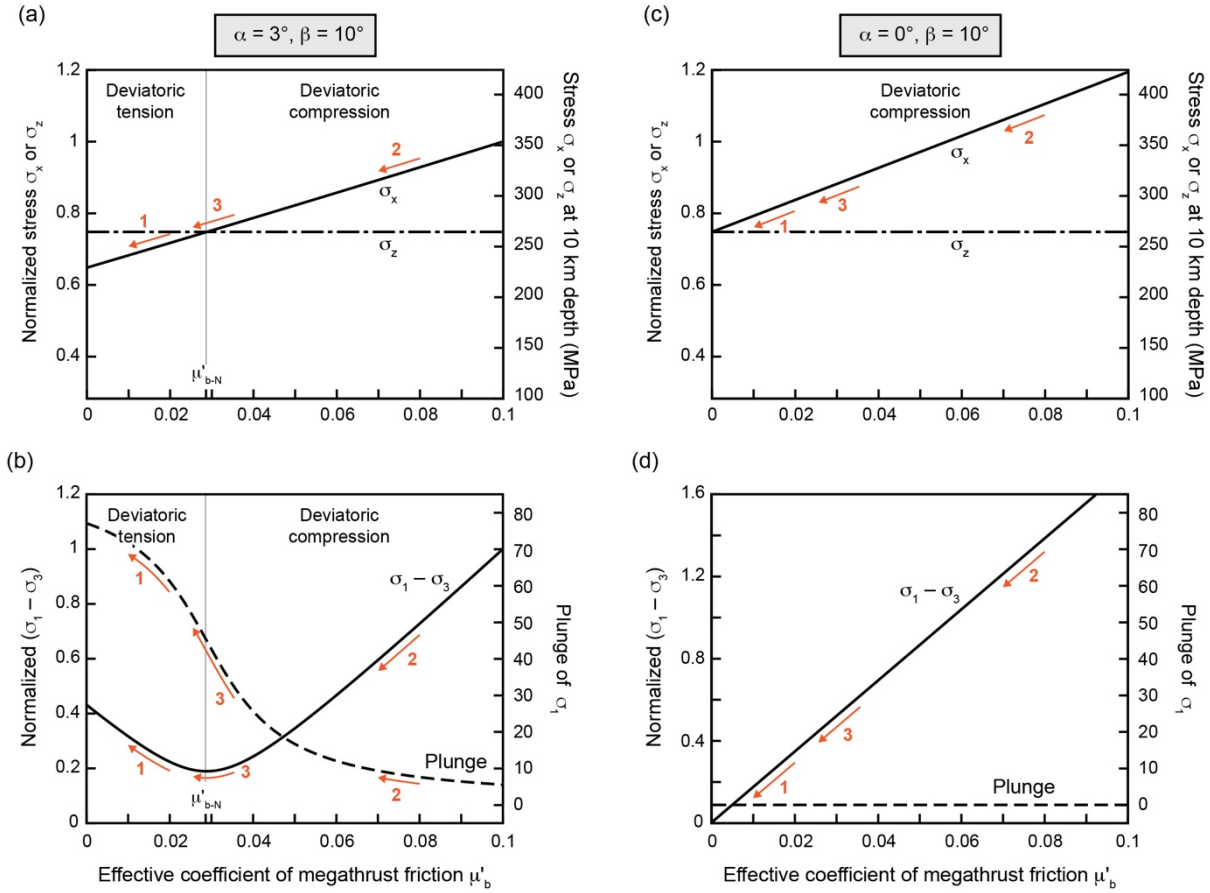
Figure 3: Analytical stress solutions for a stable dynamic Coulomb wedge. (a, b) Solutions for the reference wedge model discussed in the text. (a) Superposition of stresses σ_x and σ_z as function of effective coefficient of megathrust friction μ'_b. Parameter μ'_{b-N}
160 **denotes the μ'_b value, for which the stress state is neutral ($\sigma_x = \sigma_z$). Left ordinate shows stress values normalized to the maximum value of σ_x. Right ordinate shows total stresses at 10 km depth. (b) Differential stress ($\sigma_1 - \sigma_3$) and plunge of σ_1 as function of μ'_b. The differential stress is normalized to the maximum value of ($\sigma_1 - \sigma_3$). (c, d) Similar to (a, b) but for $\alpha = 0$. Orange arrows indicate stress changes discussed in section 2.2.**

7

For low values of μ'_b, σ_x is smaller than σ_z and the wedge is under deviatoric tension (Fig. 3a). The stress state results from the margin-normal tension induced by the topographic relief, which reduces σ_x relative to σ_z. The magnitude of σ_z results from the weight of the overburden. Increasing μ'_b increases the margin-normal compression and decreases the difference between σ_x and σ_z until both stresses are equal. At that point, the compression caused by the megathrust shear stress equals the tension induced by the topographic relief and the wedge is in a neutral state. The value of μ'_b at the neutral stress state is denoted μ'_{b-N} (dashed horizontal line in Fig. 2a) (Wang and Hu, 2006). If μ'_b is larger than μ'_{b-N}, σ_x is larger than σ_z and the wedge is under deviatoric compression (Fig. 3a).

Fig. 3b illustrates the same stress dependence in terms of differential stress ($\sigma_1 - \sigma_3$), where σ_1 and σ_3 are the greatest and least compressive principal stresses, respectively. The differential stress is a convex function of μ'_b and is minimal if the stress state is neutral, i.e., if $\mu'_b = \mu'_{b-N}$. The second ordinate in Fig. 3b shows the plunge of stress axis σ_1. The plunge decreases with increasing μ'_b from ~78° to ~6° and is 45° at the neutral stress state.

The dependence of the stress on μ'_b is similar for every wedge geometry but the value of μ'_{b-N} decreases with the surface slope angle α (Fig. S1 in Supplement). In the absence of surface slope ($\alpha = 0$), the wedge experiences no deviatoric tension and is always under deviatoric compression (Fig. 3c, d). The stress within the wedge also depends on the basal dip angle, but to a lesser extent than on the surface slope angle (Fig. S1 in Supplement).

The stress drop in a megathrust earthquake reduces the horizontal compression of the wedge, i.e., it decreases the stress σ_x (orange arrows in Fig. 3a). In the presence of surface slope, the corresponding change in differential stress varies with the effective coefficient of megathrust friction before the earthquake. The dependence is illustrated by orange arrows in Fig. 3b for a stress drop of $\Delta\mu'_b = 0.01$. The $\Delta\mu'_b$ value of 0.01 corresponds to an average stress drop of ~5 MPa at 10-30 km depth, which is compatible with estimates of rupture-zone averaged stress drops of <10 MPa (e.g., Allmann and Shearer, 2009; Brown et al., 2015; Lee et al., 2011; Luttrell et al, 2011; Kubota et al., 2022; Wang et al., 2020). When $\mu'_{b-pre} \leq \mu'_{b-N}$, the wedge is under deviatoric tension before and after the earthquake and the stress drop on the megathrust increases the differential stress because the difference between σ_x and σ_z increases (arrows 1 in Fig. 3a, b). When $\mu'_{b-pre} \gg \mu'_{b-N}$, the wedge is under deviatoric compression before and after the earthquake and stress drop decreases the differential stress because σ_x converges to σ_z (arrows 2 in Fig. 3a, b). When μ'_{b-pre} is only slightly larger than μ'_{b-N}, the megathrust stress drop may increase or decrease the differential stress within the wedge, while the stress state may switch from deviatoric compression to deviatoric tension (arrows 3 in Fig. 3a, b; Fig. 3). In the absence of surface slope, μ'_{b-pre} is always greater than μ'_{b-N} and the stress drop always decreases the differential stress in the wedge (Fig. 3c, d).

The stress change caused by the megathrust stress drop can be expressed in terms of Coulomb failure stress change to indicate whether it promotes or inhibits failure on faults within the wedge. The Coulomb failure stress on a fault plane is defined as

$$CFS = |\tau| - \mu\sigma_n \tag{3}$$

8

(e.g., Reasenberg and Simpson, 1992). The shear stress and normal stress on the fault plane are given by

$$\tau = 0.5(\sigma_1 - \sigma_3)\sin 2\omega \qquad (4a)$$

$$\sigma_n = 0.5(\sigma_1 + \sigma_3) - 0.5(\sigma_1 - \sigma_3)\cos 2\omega \qquad (4b)$$

where ω is the angle from the fault plane to the axis of σ_1, respectively. Note that the CFS considers the magnitude of the shear stress $|\tau|$, while the shear stress on a fault may be positive or negative depending on its sense of shear (e.g., King et al., 1994, Reasenberg and Simpson, 1992). In most studies, the Coulomb failure stress change is determined on faults of specified orientation, for example, on faults known from field observations, on the nodal planes of focal mechanism solutions, or on generic faults (e.g., Farias et al., 2011; Ishibe et al., 2017; Jara-Muñoz et al., 2022; Nakamura et al., 2016; Toda et al., 2011a, b). The change in Coulomb failure stress is then defined as

$$\Delta CFS_{sf} = \Delta\tau - \mu\Delta\sigma_n \qquad (5)$$

where $\Delta\tau$ is the change in shear stress (positive if slip in the direction of mainshock is promoted) and $\Delta\sigma_n$ is the change in normal stress (positive for increased compression) on the fault (e.g., Oppenheimer et al., 1988; Reasenberg and Simpson, 1992). The subscript 'sf' stands for specified fault.

Fig. 4a shows the Coulomb failure stress change resolved on a normal fault dipping at 60° toward the tip of the wedge for the reference wedge model and for $\Delta\mu'_b = 0.01$. The ΔCFS_{sf} value is always positive on the normal fault, irrespective of the $\mu'_{b\text{-pre}}$ value. In the absence of surface slope ($\alpha = 0$), the Coulomb failure stress change is larger but the trend is similar. Note that the ΔCFS_{sf} values show a weak dependence on μ'_b because σ_x depends on the factor $\mu'_b/(1 - \mu'_b)$ in a dynamic Coulomb wedge (Appendix A).

The ΔCFS_{sf} values, although mathematically correct, do not reflect that a stress drop can be stabilizing or destabilising depending on the mechanical state of the wedge (Fig. 2a), because it only depends on the relative change in σ_x. The sign of the ΔCFS_{sf} value may be correct when the investigated type of faulting agrees with the mechanical state of the wedge but the values may be misleading when the investigated type of faulting and mechanical state do not agree. For example, normal faulting is not promoted when the wedge is under deviatoric compression and the fault plane, if activated, would fail as a steep back thrust but not as a normal fault.

To take the mechanical state of the wedge into account, we determine the Coulomb failure stress change between the potential failure planes with an optimal orientation to σ_1 before the earthquake and after the earthquake. The Coulomb failure stress change can then be defined as

$$\Delta CFS_{opt} = \Delta|\tau| - \mu\Delta\sigma_n. \qquad (6)$$

The shear and normal stresses on the optimal failure planes are given by solving equation (4) for $\omega_{opt} = 0.5\tan^{-1}(1/\mu)$ (e.g., Sibson, 1998). Our determination of the Coulomb failure stress change builds on the calculations of King et al. (1994) for optimally oriented faults with the main difference, that we account for the change in the plunge of σ_1 by distinguishing between optimal failure planes after the earthquake and before the earthquake. The ΔCFS_{opt} values therefore reflect the same tendency as a change of μ'_b in the λ–μ'_b space (Fig. 2a).

9

Fig. 4b illustrates the Coulomb failure stress change between optimal failure planes for the same setting as in Fig. 4a. The Coulomb failure stress change decreases with increasing μ'_{b-pre}, with its magnitude and sign being mainly controlled by the stress state in the wedge. The Coulomb failure stress change is positive if the wedge is under deviatoric tension before and after the earthquake (i.e., if $\mu'_{b-pre} \leq \mu'_{b-N}$), in which case the decrease in σ_x and increase in $(\sigma_1 - \sigma_3)$ promote normal faulting. Conversely, the Coulomb failure stress change is negative if the wedge is under deviatoric compression before and after the earthquake (i.e., if $\mu'_{b-pre} \gg \mu'_{b-N}$), in which case the decrease in σ_x and $(\sigma_1 - \sigma_3)$ inhibit thrust faulting. Note that ΔCFS_{opt} can be positive if μ'_{b-pre} is only slightly larger than μ'_{b-N}. In that case, the plunge of σ_1 is close to 45° after the earthquake and the Coulomb failure stress change promotes thrust faulting on one of the failure planes (the steeper one) and normal faulting on the other (see also Fig. 2a). In the absence of surface slope ($\alpha = 0$), ΔCFS_{opt} is always negative, because the wedge cannot attain a state of deviatoric tension and normal faulting is never promoted (Fig. 2b, d). The Coulomb failure stress change further increases with the magnitude of the stress drop (Fig. 4c) and with the coefficient of friction μ (Fig. 4d).

It should be noted that Fig. 4 illustrates the Coulomb failure stress changes due to a 'positive' stress drop on the megathrust, i.e., a decrease in megathrust shear stress. A negative stress drop, i.e., an increase in megathrust shear stress, has the opposite effect on the total stresses in the wedge and the corresponding Coulomb failure stress changes (see Fig. S2 in the Supplement). An increase in megathrust shear stress tends to inhibit normal faulting if the wedge is under deviatoric tension and to promote thrust faulting if the wedge is under deviatoric compression. In nature, negative stress drops contribute to arrest the earthquake rupture and may occur downdip and updip of the main rupture area or along velocity strengthening patches enclosed in the main rupture area (e.g., Bilek and Lay, 2002; Brown et al., 2015; Luttrell et al. 2011; Wang and Hu, 2006; Wang et al., 2020).
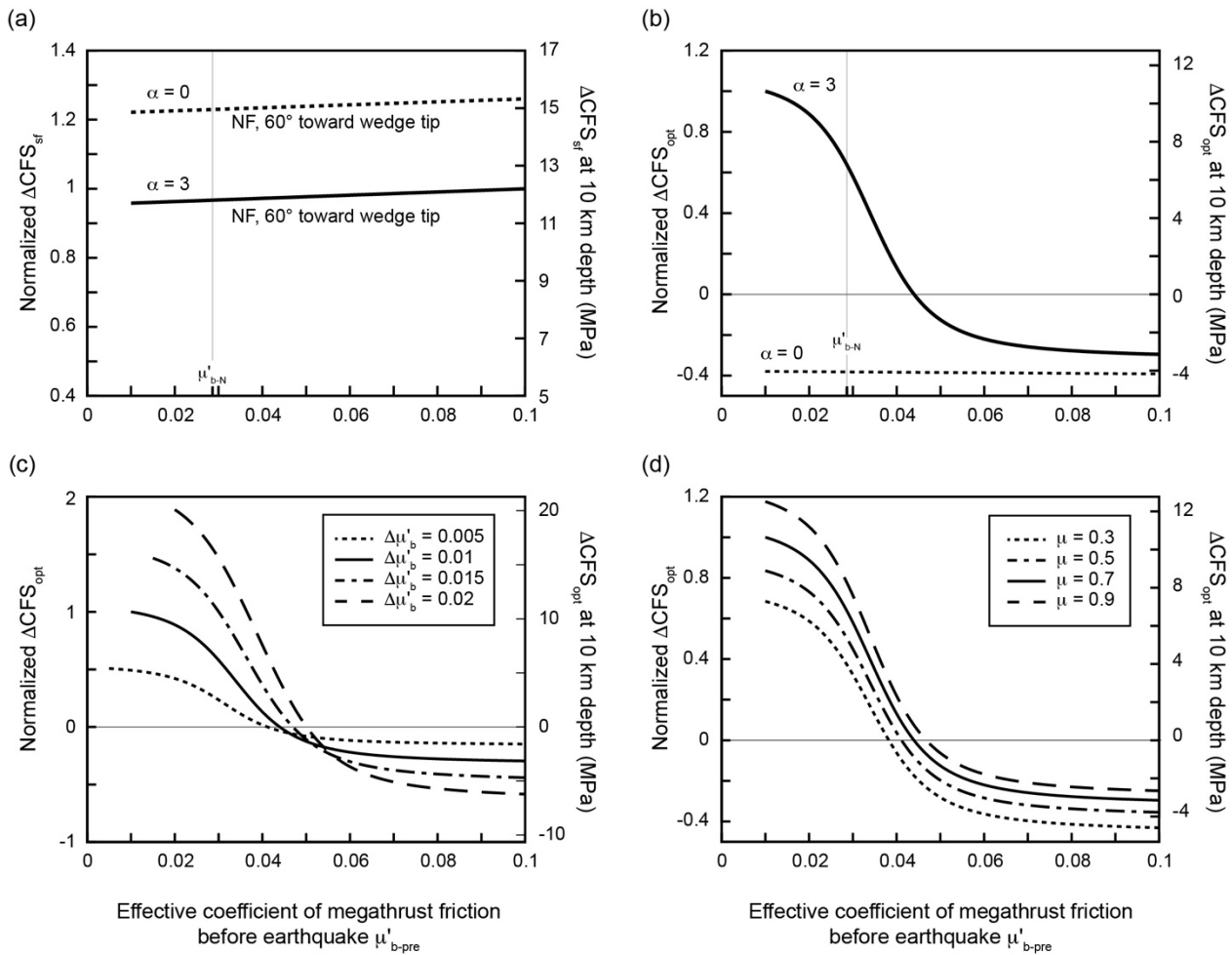
Figure 4: Coulomb failure stress change as function of effective coefficient of megathrust friction before the earthquake, $\mu'_{b\text{-pre}}$, and for a change in megathrust friction of $\Delta\mu'_b = 0.01$. Solid lines indicate solutions for the reference wedge model discussed in the text. Dashed and dotted lines indicate solutions for adjusted model parameters. (a) Coulomb failure stress change on a normal fault (NF) dipping at 60° toward the wedge tip. (b) Difference in Coulomb failure stress on optimal failure planes before and after the earthquake, ΔCFS_{opt}. (c, d) Dependence of ΔCFS_{opt} on $\Delta\mu'_b$ and coefficient of friction μ. Left ordinates show ΔCFS values normalized to the maximum ΔCFS value obtained for reference wedge model. Right ordinate indicates ΔCFS values at 10 km depth. All ΔCFS values in (a-c) are calculated for $\mu = 0.7$.

3 Assessment of Coulomb failure stress changes caused by the Tohoku-Oki and Maule megathrust earthquakes

We showed in section 2 that the tendency of a megathrust earthquake to promote or inhibit failure in the wedge depends on the mechanical state of the wedge. Failure is promoted if the wedge is close to a neutral state or under deviatoric tension after the earthquake. Whether the earthquake results in such a stress state depends on the magnitude of the stress drop and on the stress state before the earthquake, and requires the presence of topographic relief. The mechanical state, the megathrust stress drop, and the forearc topography all vary along strike and across the plate margin. The Coulomb failure stress change

11

therefore differs with the location in the forearc, which needs to be taken into account when assessing ΔCFS_{opt} for megathrust earthquakes.

265 In the following, we determine the Coulomb failure stress changes caused by the 2011 M_w 9.0 Tohoku-Oki earthquake, Japan, and the 2010 M_w 8.8 Maule earthquake, Chile, using plane-strain finite-element models of force balance. The models consider the interaction of topographic and tectonic stresses, like the Coulomb wedge model, but allow to take into account spatial variability in stress state, stress drop, and topography across the plate margin. We construct for each megathrust earthquake individual finite-element models for two sections across the forearc. The cross sections are oriented

270 perpendicular to the plate margin and cover the area of the megathrust earthquake hypocentre and the area of most intense aftershock seismicity in the forearc (Sendai and Iwaki cross sections in Fig. 5, and Pichilemu and Concepción cross sections in Fig. 6).

3.1 Model setup

The finite-element models are based on the modelling approaches of Wang et al. (2019) and Dielforder et al. (2023) and

275 yield the total stresses in a forearc resulting from gravity, forearc topography and the shear stress on the megathrust (Fig. 1c). The models are created with the commercial finite-element software ABAQUS (version 2018) and comprise a rigid lower plate in frictional contact with an elastic upper plate that is subdivided into continental crust and mantle. Following previous studies (Dielforder et al., 2023; Dielforder and Hampel, 2021; Wang et al., 2019; Wang and He, 1999), we adopt a nearly incompressible material for the upper plate (Poisson ratio ν = 0.48) and densities of 1025 kg/m^3, 2800 kg/m^3, and 3300

280 kg/m^3 for water, crust, and mantle respectively. We note that using a different Poisson's ratio (e.g., ν = 0.3) makes little difference to the model results (cf. Dielforder and Hampel, 2021). The Young's moduli for crust and mantle are 60 GPa and 150 GPa, respectively. A lithostatic pressure and an elastic foundation are applied to the bottom of the model to implement isostasy (arrows and springs in Fig. 1c). The right-hand side of the model (back side of the upper plate) is free to move vertically but is fixed in the horizontal direction. All models are meshed with linear tetrahedral elements with an average

285 element edge length of ~1 km. The margin topography is approximated by the mean elevation, which we calculate from the ETOPO1 global relief model using TopoToolbox for MATLAB (Amante and Eakins, 2009; Schwanghart and Scherler, 2014). The slab geometry is approximated by fitting an arc with constant curvature through the upper 80 km of the Slab2 model (Hayes et al., 2018).

The megathrust is implemented as a frictional contact between the upper and lower plates and extends from the trench down

290 to a depth of 60 km. The shear stress on the megathrust obeys the friction law for a cohesionless fault and is generated by displacing the lower plate in downdip direction tangential to the plate interface. The displacement ensures that the entire plate interface is at a state of failure (cf. Wang and He, 1999). The stress and strain in the upper plate are independent of the total displacement of the lower plate. The coefficient of megathrust friction can vary along the megathrust, which allows a detailed control on stress magnitudes. In nature, the megathrust transitions into a viscous shear zone downdip of the

295 seismogenic zone, with the shear stress decreasing towards zero with depth (Lamb, 2006; Wada and Wang, 2009). We

12

implement the transition zone in the models as frictional contact between the downdip limit of the megathrust and 80 km depth (cf. Dielforder and Hampel, 2021). The μ'_b value of the transition zone is set to 0.001, which results in a low shear stress of 2-3 MPa. Below a depth of 80 km, the contact between the lower and upper plates is frictionless, i.e., the shear stress on the contact is zero.

300 Each model run includes three analysis steps. In the first step, a lithostatic prestress is assigned, gravity is applied, and isostatic equilibrium is established. The prestress facilitates the computation of the total stresses resulting from the boundary conditions. The second and third analysis steps are used to calculate the total stresses in the forearc just before and after the earthquake, similar to the pre-earthquake and post-earthquake steps in the dynamic Coulomb wedge model. In the second analysis step, the $\mu'_{b\text{-}pre}$ values are assigned to the megathrust and the lower plate is displaced. At that stage, ABAQUS yields

305 the total stresses in the upper plate for the pre-earthquake configuration. In the third analysis step, the $\mu'_{b\text{-}post}$ values are assigned to the megathrust, the lower plate is displaced, and ABAQUS yields the total stresses in the upper plate for the post-earthquake configuration.

3.2 Estimation of forearc stress states and megathrust stress drop

The calculation of ΔCFS_{opt} requires an estimation of the forearc stress state before and after the earthquake. If the megathrust

310 stress drop is given, one of the stress states can be estimated from the other. Here, we estimate the stress states using the following procedure (cf. Wang et al., 2019). We first calculate the mean stress drop along the cross sections using published stress-drop models and determine the corresponding $\Delta\mu'_b$ values. For the Tohoku-Oki earthquake, we use the stress drop-model of Brown et al. (2015) for the coseismic-slip model of Iinuma et al. (2012) (Fig. 5b, d). For the Maule earthquake, we use the stress-drop model of Luttrell et al. (2011) for the coseismic-slip model of the same authors (Fig. 6b, d). We then use

315 μ'_b values derived from heat-dissipation models (Gao and Wang, 2014) and force balance models (Dielforder, 2017; Lamb, 2006) as an initial estimate of $\mu'_{b\text{-}pre}$ (applied in model step 2). The μ'_b values estimate the apparent strength of the megathrust, i.e., the level of shear stress that the fault can sustain before great earthquakes (heat-dissipation models) and that is required to prevent the continental-margin relief from gravitational collapse (force-balance models). Both modelling approaches yield comparable μ'_b values of about 0.03±0.01 for the Japanese and Chilean megathrusts (Dielforder, 2017; Gao

320 and Wang, 2014; Lamb, 2006). Subtracting the $\Delta\mu'_b$ values obtained from the megathrust stress drop from the $\mu'_{b\text{-}pre}$ values yields an estimation of the $\mu'_{b\text{-}post}$ values (applied in model step 3).

We then solve the finite element model and evaluate whether the post-earthquake stress state is compatible with focal mechanisms of upper-plate earthquakes that occurred within the 50-km-wide swath profiles in the first year after the megathrust earthquake (Figs. 5c and 6c). The focal mechanisms are from the Japan Meteorological Agency and from the

325 earthquake catalogue of Şen et al. (2015) for Japan and Chile, respectively. We assume that the modelled stress state is compatible with focal mechanism solutions, if thrust faulting and normal faulting events occur in areas of deviatoric compression and deviatoric tension, respectively. A near-neutral stress state (plunge of σ_1 between 40-50°) is considered to

be consistent with both thrust faulting and normal faulting. If the stress state and focal mechanism are not compatible, we adjust the $\mu'_{b\text{-pre}}$ values, determine the corresponding $\mu'_{b\text{-post}}$ values, and solve the model again.

330 We repeat the procedure until the stress state after the earthquake agrees with the majority of the focal mechanisms. We thereby obtain an estimation of the total stresses in the forearc and corresponding megathrust shear stresses shortly before and after the megathrust earthquakes that is consistent with the stress-drop models and the post-mainshock fault kinematics in the forearc. The forearc stress states in the interseismic periods before and after the mainshock are not determined and do not influence the calculation of the coseismic Coulomb failure stress change. However, it should be noted that most of the

335 post-mainshock focal mechanisms indicate normal faulting, some of which may have been caused by afterslip and aftershocks on the megathrust in the postseismic period (e.g., Bedford et al., 2016; Nakamura et al., 2016; Sun et al., 2014). Such events may record stress release on the megathrust in addition to the coseismic stress drop and influence our assessment of the post-seismic stress state. We expect this potential effect to be small on our calculations because the normal faulting started soon after the mainshocks (e.g., Farías et al., 2011; Lange et al., 2012; Yoshida et al., 2012; Japan

340 Meteorological Agency) and affected always the same forearc areas in the first postseismic year (Figs. S3 and S4 in Supplement).

The procedure of estimating the pre-earthquake and post-earthquake stress states is similar for all models, except for the Concepción model crossing the hypocentre location of the Maule earthquake, for which the fault kinematics in the forearc are poorly constrained by focal mechanisms (Fig. 6c). We therefore calculate the Coulomb failure stress change for the

345 Concepción model for the initial estimate of μ'_b of 0.03 derived from heat-dissipation models (Gao and Wang, 2014).
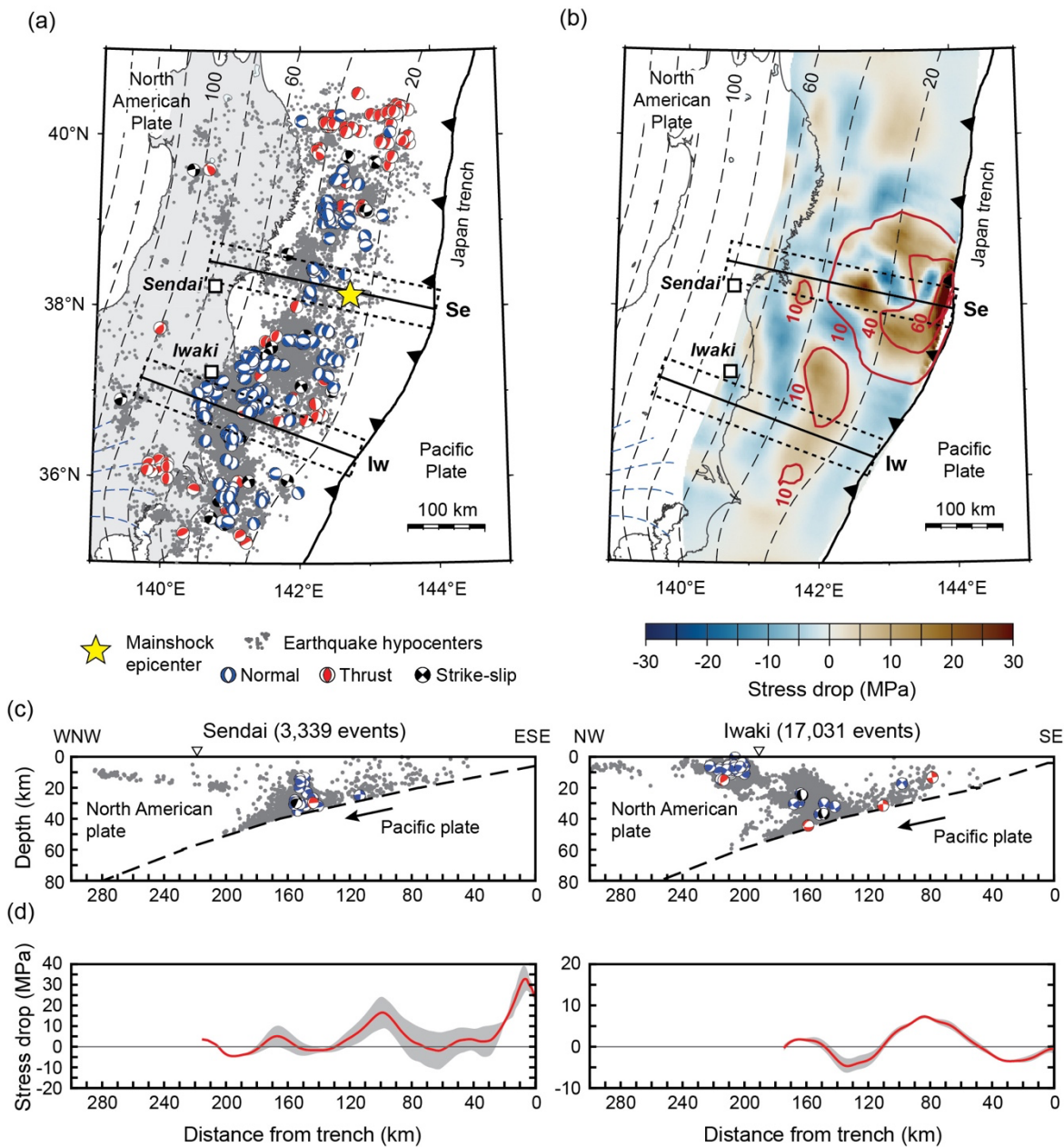
14

Figure 5: Seismotectonic setting of northeast Japan. (a) Seismicity in the upper (North American) plate after the 2011 M_w 9.0 Tohoku-Oki earthquake (yellow star). Grey dots are aftershock hypocentres from the Japan Meteorological Agency (JMA). All events have a magnitude ≥ magnitude of completeness of 1.5 (determined with the maximum curvature method of Wiemer and Katsumata, 1999). Beach balls denote JMA focal mechanism solutions. (b) Earthquake slip contours in meter (pink lines and numbers) and coseismic megathrust stress drop (blue to red colour bar signal). Slip contours and stress drop from Iinuma et al. (2012) and Brown et al. (2015), respectively. (a, b). Black lines indicate location of cross sections shown in (c, d). Dashed rectangles indicate the width of swaths (50 km) used to evaluate the seismicity distribution and fault kinematics (c) and the average stress drop on the megathrust (d) along the Sendai (Se) and Iwaki (Iw) cross sections.

15
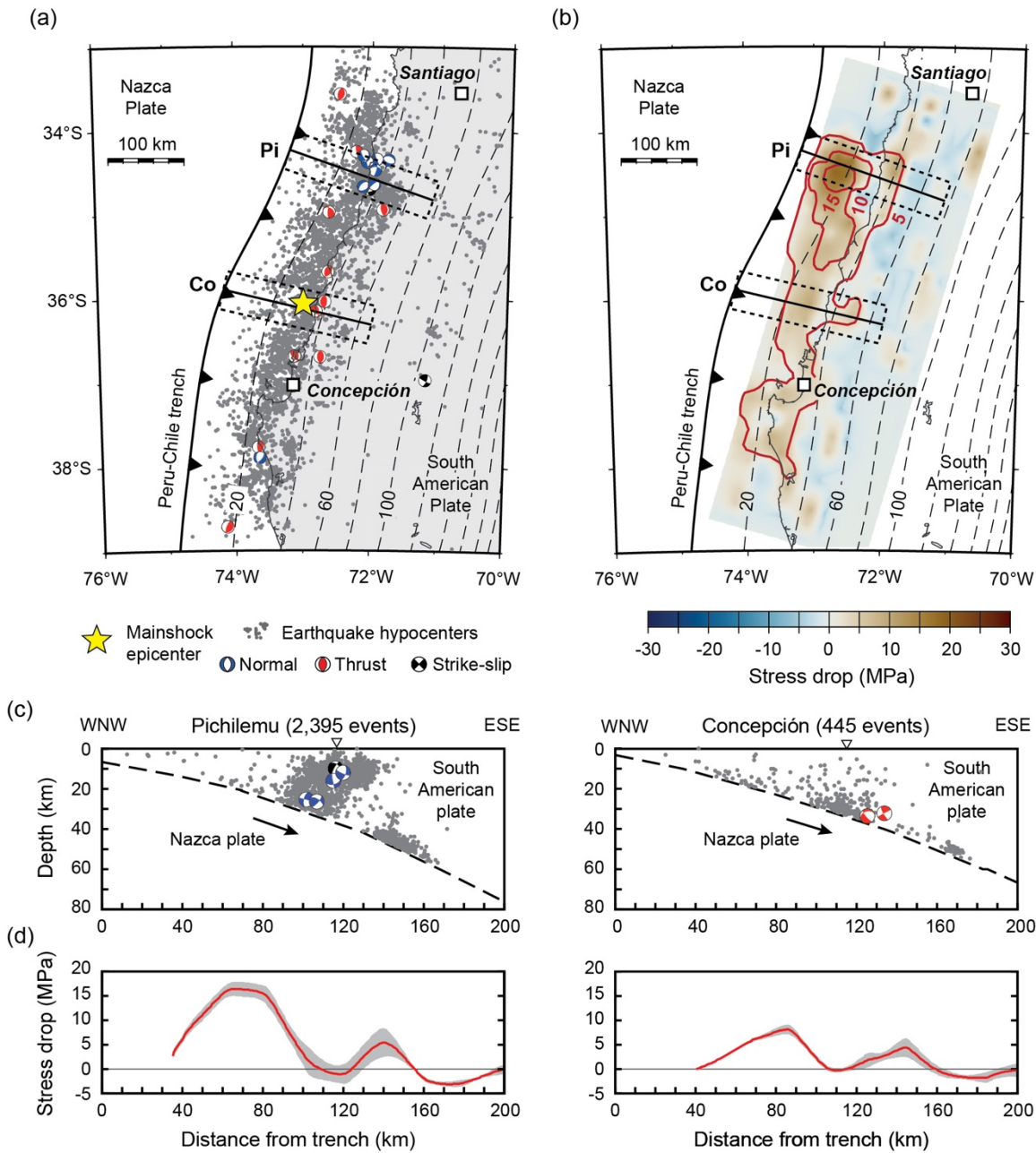
Figure 6: Seismotectonic setting of south-central Chile. (a) Seismicity in the upper (South American) plate after the 2010 M_w 8.8 Maule earthquake (yellow star). Grey dots are aftershock hypocentres from Lange et al. (2012). All events have a magnitude ≥ magnitude of completeness of 2.0 (determined with the maximum curvature method of Wiemer and Katsumata, 1999). Beach balls denote focal mechanism solutions from Şen et al (2015). (b) Earthquake slip contours in meter (pink lines and numbers) and coseismic megathrust stress drop (blue to red colour bar signal). Slip contours and stress drop from Luttrell et al. (2011). (a, b). Black lines indicate location of cross sections shown in (c, d). Dashed rectangles indicate the width of swaths (50 km) used to evaluate the seismicity distribution and fault kinematics (c) and the average stress drop on the megathrust (d) along the Pichilemu (Pi) and Concepción (Co) cross sections.

16

4 Results of the finite-element models

The main modelling results are presented in Figs. 7-10. Supplementary modelling results for alternative stress drop models and model parameters are shown in Fig. 11 and Figs. S5-S14 in the Supplement and will be discussed in section 5. The forearc stresses before and after the earthquake as well as the incremental stress change caused by the earthquake are

370   illustrated in terms of 2-D deviatoric stress, i.e., the hydrostatic stress $(\sigma_x + \sigma_z)/2$ has been subtracted from the stress tensor (cf. Wang et al., 2019). The Coulomb failure stress changes reported in Figs. 7-10 are computed from the total stresses following equation (6) and for $\mu = 0.7$.

4.1 Results for the 2011 M$_w$ 9.0 Tohoku-Oki earthquake

4.1.1 Sendai cross section

375   Fig. 7 shows the preferred model of forearc stress change due to the Tohoku-Oki earthquake for the Sendai cross section. The forearc experiences almost everywhere deviatoric compression before the earthquake (red crosses in Fig. 7a). The stress drop on the megathrust reduces the compression in the entire forearc (blue crosses in Fig. 7b). After the earthquake, the stress state is more heterogeneous and the forearc experiences deviatoric tension between 0 and ~220 km and at ~280-300 km from the trench (blue crosses in Fig. 8c). The extent of deviatoric tension in the model is compatible with the normal-

380   faulting focal mechanisms between ~110-160 km from the trench (Figs. 5c and 7c), but not with the thrust-faulting focal mechanism at ~140 km from the trench. This event has a potential failure plane parallel to the plate interface and we interpret it as an event on the megathrust (cf. Nakamura et al., 2016). Alternatively, the event may indicate a local stress heterogeneity that we cannot reproduce in our models.

The modelled megathrust shear stresses before and after the Tohoku-Oki earthquake and the modelled megathrust stress drop

385   are shown in Fig. 7d. Before the earthquake, the megathrust shear stress tends to increase with distance from the trench (i.e., depth along the fault), except near the trench, where the shear stress is comparatively high. The shear stress values relate to $\mu'_{\text{b-pre}}$ values of 0.015 to 0.022, except for the shallowest portion of the megathrust within 10 km from the trench, for which $\mu'_b = 0.2$. The elevated $\mu'_{\text{b-pre}}$ value near the trench is required to allow for a large stress drop on the shallowest part of the megathrust related to the large fault slip of ≥60m near the trench (Fig. 5a) and causes the strong compression near the trench

390   before the earthquake (large stress crosses in Fig. 7a, b). Note that high stress drop near the trench may be an artifact inherited from the rupture model of Iinuma et al. (2012), a point we will revisit in section 5.2. After the earthquake, the megathrust shear stress is more heterogeneous and reaches zero at ~0-40 km and ~100 km from the trench, indicating locally complete stress drops (e.g., Brodsky et al., 2020; Hasegawa et al., 2011). The corresponding $\mu'_{\text{b-post}}$ vary between 0 and 0.025 along the megathrust. The $\Delta\mu'_b$ values vary between -0.005 and 0.022, except for the shallowest portion of the megathrust,

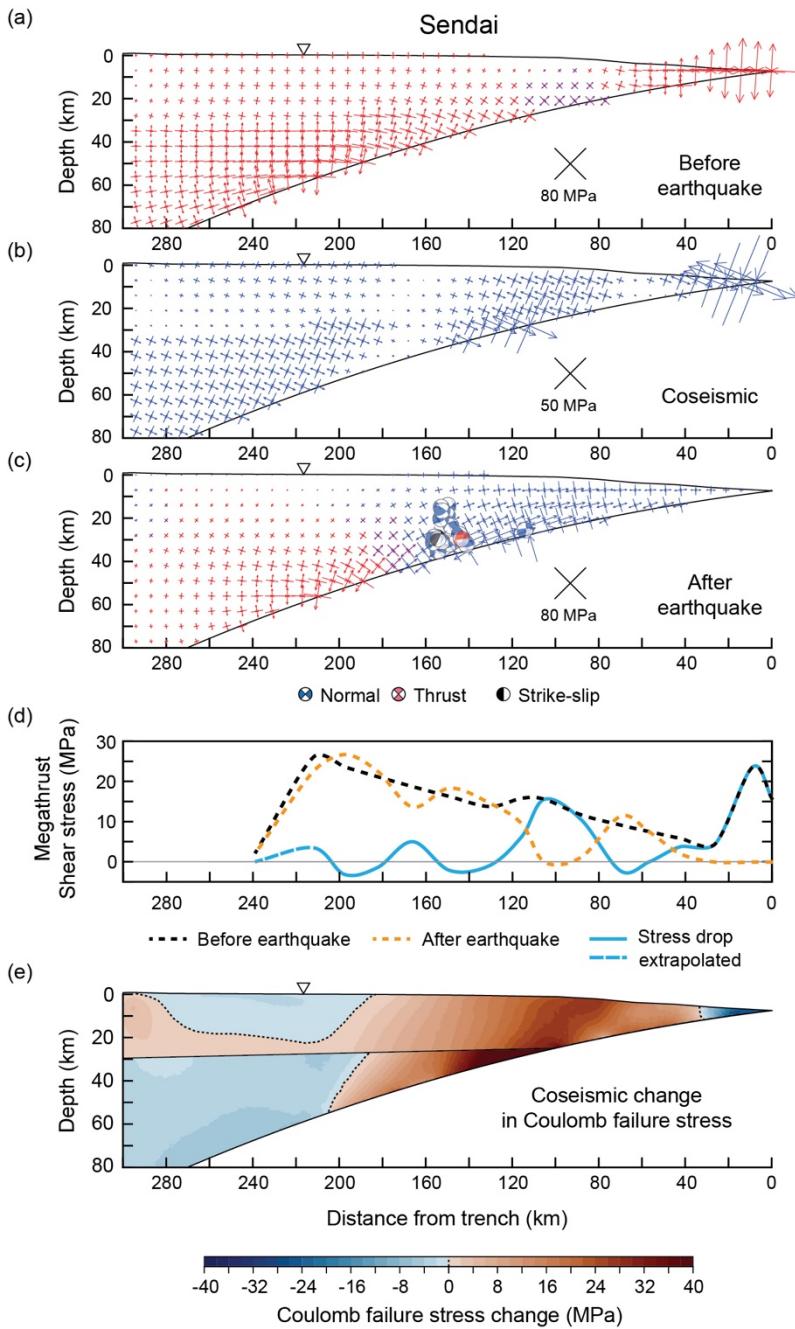395   for which $\Delta\mu'_b = 0.2$.

Figure 7: Preferred model of forearc stress change due to the Tohoku-Oki earthquake along the Sendai cross section. See Fig. 5a for the location of the cross section. Red and blue stress crosses in (a-c) indicate that the plunge of σ_1 is less than 40° (deviatoric compression) and more than 50° (deviatoric tension), respectively; purple crosses indicate a plunge of σ_1 between 40° and 50°. The size of the stress crosses scale with the differential stress. (a) Deviatoric stress before the earthquake. (b) Incremental change in deviatoric stress caused by the earthquake. (c) Deviatoric stress after the earthquake. Beach balls indicate focal mechanism solutions of aftershocks (cf. Fig. 5). (d) Modelled megathrust shear stress before (black) and after (orange) the earthquake, and megathrust stress drop (blue). (e) Coseismic change in Coulomb failure stress calculated for $\mu = 0.7$.

400

4.1.2 Iwaki cross section

405   The stress state in the forearc along the Iwaki cross section is heterogenous before the earthquake (Fig. 8a). Most of the submarine forearc is in a neutral stress state (plunge of σ_1 40-50°) or under deviatoric tension, which is compatible with mixed reverse and thrust faulting reported for the years before the Tohoku-Oki earthquake (e.g., Hasegawa et al., 2012; Nakamura et al., 2016; Yoshida et al., 2012). At greater distance to the trench, larger forearc areas are under deviatoric compression. The megathrust stress drop decreases the horizontal compression in the forearc, and reverses the stress state

410   from deviatoric tension to deviatoric compression within ~60 km from the trench except near the trench, where the compression increases (Fig. 8b).

The modelled extent of deviatoric tension after the earthquake is compatible with the majority of the normal-faulting focal mechanisms between ~100 and ~230 km from the trench (Figs. 5c and 8c). There is one normal-faulting focal mechanism at ~170 km from the trench occurring in an area of deviatoric compression. Thrust faulting events at ~80 and ~110 km from the

415   trench have potential failure planes parallel to the plate interface and are interpreted as megathrust events. In contrast, the thrust faulting events at ~160 and ~215 km from the trench have potential failure planes oblique to the plate interface and are likely upper-plate events. In particular, the thrust faulting at ~215 km from the trench, directly beneath the normal faulting events in the upper crust has been constrained by detailed moment tensor inversion (Yoshida et al., 2015). Both, the thrust faulting near the plate interface, at 160 km from the trench and in the lower crust, at ~215 km from the trench are compatible

420   with the modelling results (Fig. 8c).

The modelled megathrust shear stress increases with depth along the fault before the megathrust earthquake (Fig. 8d). The corresponding $\mu'_{b\text{-pre}}$ values vary between 0.02 and 0.023. There is no local peak in megathrust shear stress near the trench as for the Sendai cross section. After the megathrust earthquake, the shear stress is more heterogenous due to the stress drop, which is nowhere complete and smaller than for the Sendai cross section (Fig. 5b, d). The $\mu'_{b\text{-post}}$ and $\Delta\mu'_b$ values vary

425   between 0.008–0.036 and -0.015–0.013, respectively. The stress drop on the megathrust causes changes in Coulomb failure stress of -10 and +12 MPa (Fig. 8e). Areas of positive ΔCFS include most of the forearc crust at >80 km from the trench and much of the mantle wedge between 100 and 240 km from the trench. The Coulomb failure stress mainly decreases in the submarine forearc at 40–80 km from the trench and in the mantle wedge at >240 km. The areas of Coulomb failure stress increase contain ~98 % of the forearc seismicity along the Iwaki cross section (Fig. 10).
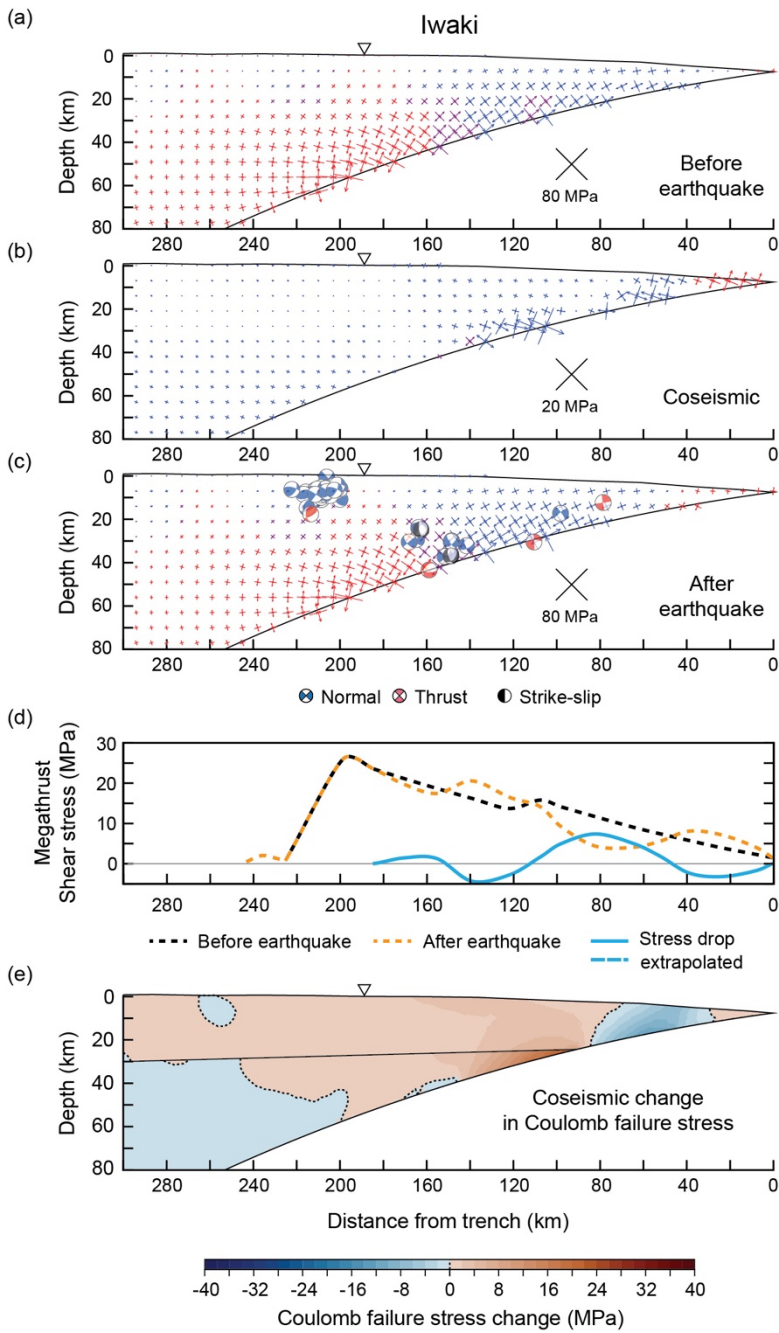
430

Figure 8: Preferred model of forearc stress change due to the Tohoku-Oki earthquake along the Iwaki cross section. See Fig. 5a for the location of the cross section. The meaning of panels (a-e) is the same as in Fig. 7. The coseismic change in Coulomb failure stress in (e) is calculated for μ = 0.7.

435

## 4.2 Results for the 2010 M_w 8.8 Maule earthquake

4.2.1 Pichilemu cross section

The forearc along the Pichilemu transect experiences mainly deviatoric compression before the Maule earthquake (Fig. 9a).
The stress drop on the megathrust decreases the horizontal compression in the entire forearc (Fig. 9b) and reverses the stress
state from deviatoric compression to deviatoric tension within ~20 to 130 km from the trench (Fig. 9c). The extent of
deviatoric tension in the model is compatible with the normal-faulting focal mechanisms between ~100 and 130 km from the
trench (Figs. 6c and 9c). The modelled megathrust shear stress before the earthquake increases along the fault to about ~20
MPa and then fluctuates by a few MPa before decreasing toward zero at >120 km from the trench, i.e., at a depth >40 km
(Fig. 9d). The corresponding $\mu'_{b\text{-pre}}$ values vary between 0.043 and 0.02 at 5–40 km depth, and between 0.02 and 0.005 at 40–
60 km depth (i.e., the coefficient of megathrust friction tends to decrease with depth). The stress drop on the megathrust is
near complete at ~60–80 km from the trench where the shear stress on the megathrust approaches zero after the earthquake.
The $\mu'_{b\text{-post}}$ and $\Delta\mu'_b$ values vary between 0.006–0.04 and -0.002–0.036, respectively. It should be noted that the stress drop
within 40 km from the trench is not well constrained (Fig. 5b) due to the lack of seafloor geodetic observations and is here
assumed to decrease to zero toward the trench (dashed part in Fig. 9d).

The stress change in the forearc causes changes in Coulomb failure stress of -10 and +18 MPa (Fig. 9e). The Coulomb
failure stress increases almost everywhere in the forearc at except for some areas along the megathrust and in the upper
forearc crust between ~130 and 200 km from the trench. The areas of Coulomb failure stress increase contain ~87 % of the
forearc seismicity along the Pichilemu transect (Fig. 10).

4.2.2 Concepción cross section

The forearc along the Concepción cross section experiences mainly deviatoric compression before the Maule earthquake,
except between ~20 and 50 km from the trench (Fig. 9a). The stress drop on the megathrust decreases the horizontal
compression in the entire forearc except near the trench, where the compression slightly increases (Fig. 9b). After the
earthquake, deviatoric tension occurs up to ~70 km from the trench (Fig. 9c). Further landward the forearc remains under
deviatoric compression, which agrees with two thrust-faulting focal mechanisms at about 120–130 km from trench (Figs. 6c
and 9c). Both events have potential failure planes oblique to the plate interface and are interpreted as events in the mantle
wedge above the megathrust.

21
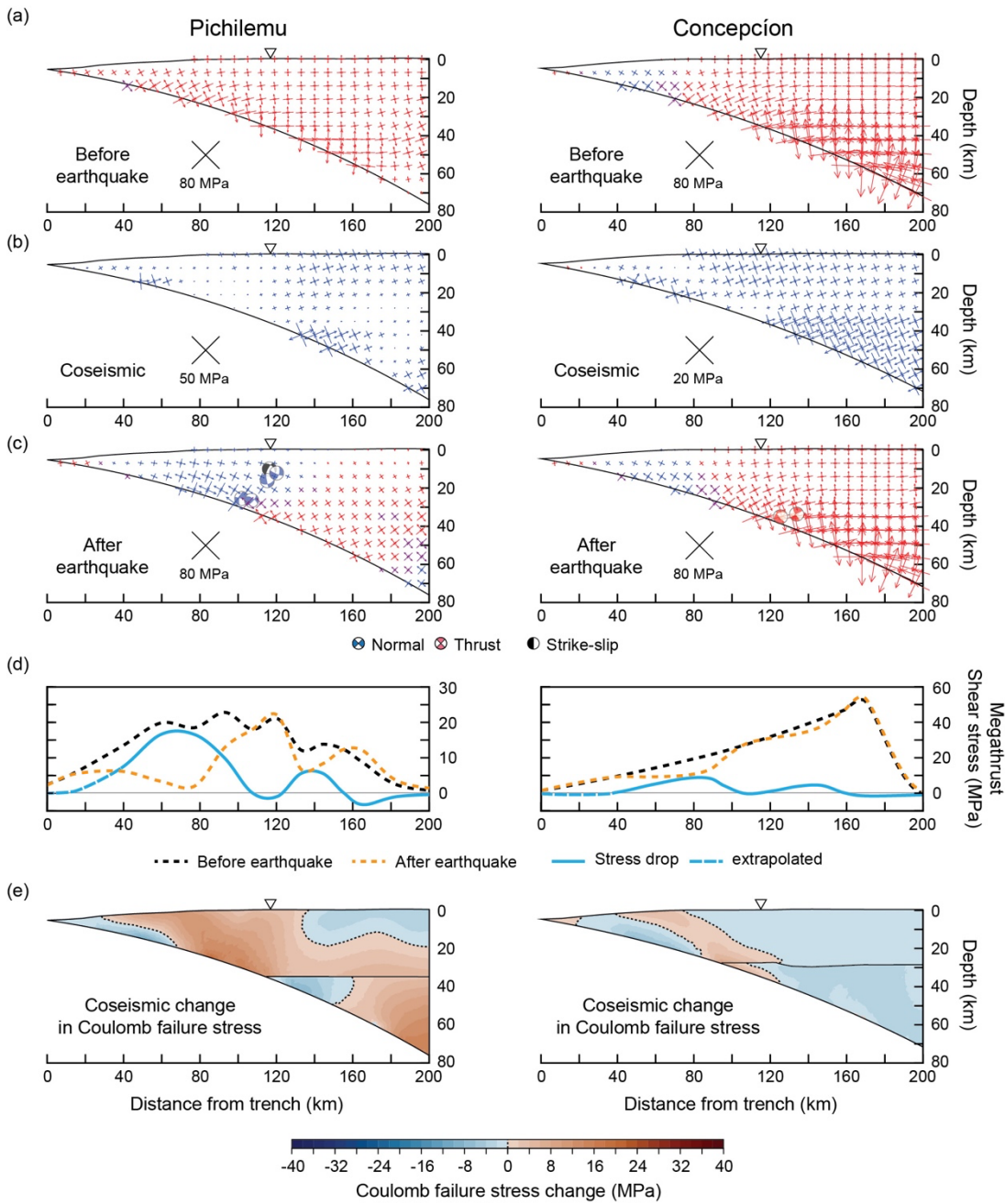
Figure 9: Preferred model of forearc stress change due to the Maule earthquake along the Pichilemu (left) and Concepcíon (right) cross sections. See Fig. 6a for the location of the cross sections. The meaning of panels (a-e) is the same as in Fig. 7. The coseismic change in Coulomb failure stress in (e) is calculated for $\mu = 0.7$.

The shear stress on the megathrust before the earthquake increases with distance from the trench to about 50 MPa at the
470 downdip limit of the megathrust (~170 km from the trench) (Fig. 9d). The steady increase in megathrust shear stress reflects
the constant μ'_{b-pre} value of 0.03. The largest stress drop of ~8 MPa occurs at about 80 km from the trench, close to the
hypocentre of the Maule earthquake (Figs. 6a and 9d). The stress drop is smaller than for the Pichilemu cross section and is
nowhere complete. The μ'_{b-post} and $\Delta\mu'_b$ values vary between 0.016–0.035 and -0.005–0.014, respectively.

The stress drop causes changes in Coulomb failure stress from -6 to +6 MPa (Fig. 9e). The areas of Coulomb failure stress
475 increase contain ~64 % of the forearc seismicity along the Concepción cross section (Fig. 10).
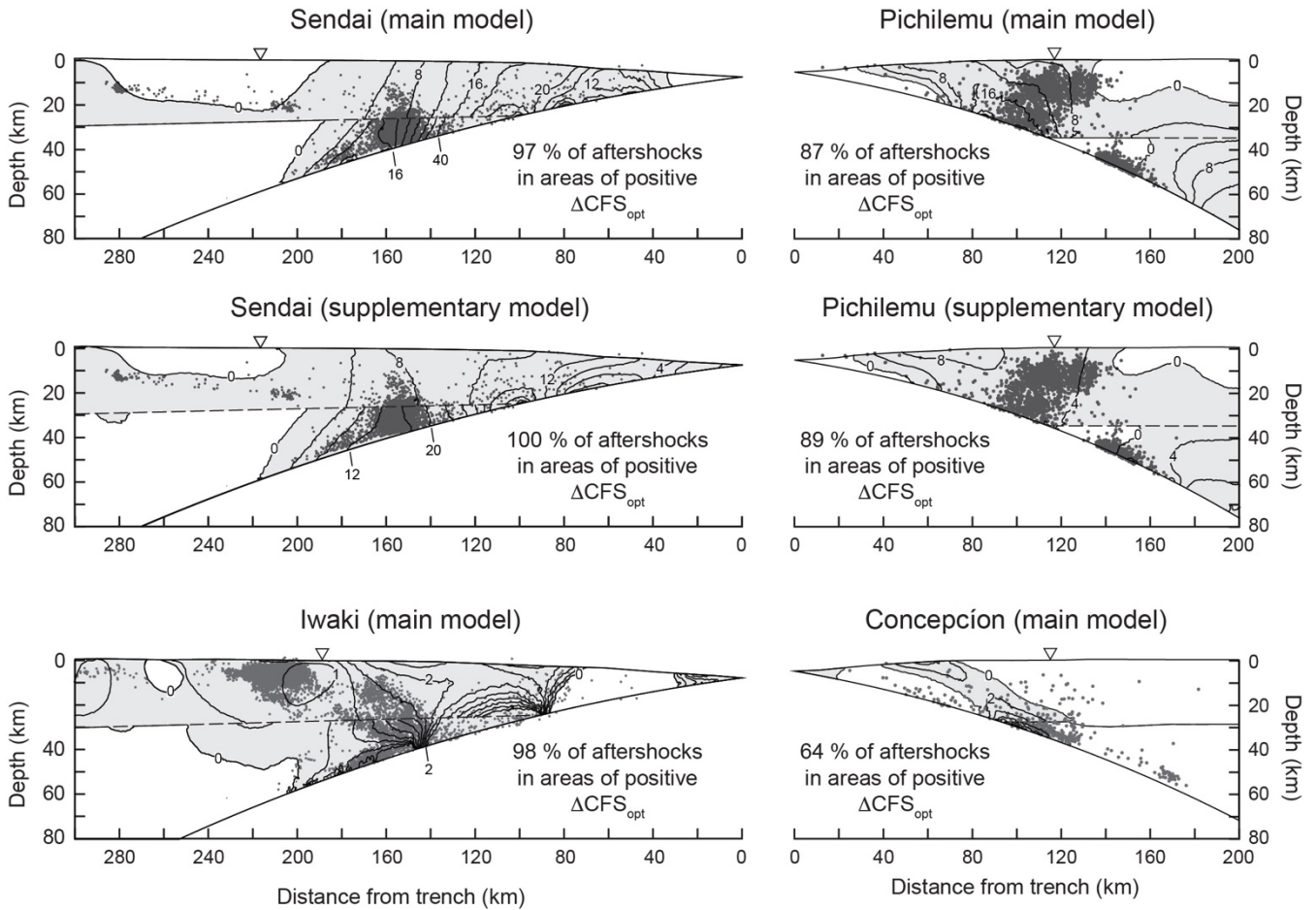
**Figure 10: Earthquake hypocentres (grey dots) within 50-km-wide swath profiles projected onto the plane cross-section. See Figs.
480 5a and 6a for location of swath profiles. Grey areas indicated areas of positive Coulomb failure stress increase as in Figs. 7e-9e and
11e. Black contour lines in step of 4 MPa (Sendai, Pichilemu), 2 MPa (Concepcíon), and 0.5 MPa for Iwaki. Main model results for
the stress drop models of Brown et al. (2015) for Japan (Sendai, Iwaki) and of Luttrell et al. 2011 for Chile (Pichilemu,
Concepcion). Supplementary model results for the stress drop models of Kubota et al. (2022) for Sendai and of Wang et al. (2020)
for Pichilemu.**

23

5 Discussion

5.1 Main factors controlling failure after large megathrust earthquakes

We use analytical stress solutions of the dynamic Coulomb wedge theory (Wang and Hu, 2006) and numerical finite-element models of force balance (Dielforder et al., 2023; Wang et al., 2019) to investigate coseismic Coulomb failure stress changes caused by a megathrust earthquake in the forearc. The Coulomb failure stress change is determined as difference in Coulomb failure stress on the pre-earthquake and post-earthquake optimal failure planes and takes into account the total stresses in the forearc and the resulting mechanical state.

The mechanical state of a forearc is crucial for understanding the conditions under which the stress drop in megathrust earthquakes may trigger failure in the forearc. Widespread failure is only promoted, if the megathrust shear stress before the earthquake is so low that the compression of the forearc is not much higher than the deviatoric tension due to topographic relief. At this condition, the forearc is close to a neutral state and the megathrust stress drop can increase the deviatoric tension in the forearc which promotes failure. If the forearc compression is much higher than the deviatoric tension due to topographic relief, the megathrust stress drop only decreases the compression, which inhibits failure.

The near-neutral stress conditions required for failure agree with independent estimates of forearc stresses. Force balance analyses of global subduction zones indicates that near-neutral stress conditions are given for effective coefficients of megathrust friction of ~0.03±0.02 (Dielforder et al., 2020; Lamb, 2006; Matthies et al., 2024; Seno, 2009). The μ'_b values from force-balance models are consistent with estimates of μ'_b derived from other methods, including heat-dissipation models (e.g., Bird, 1978; Gao and Wang, 2014; van den Beukel and Wortel, 1987, 1988, Wada and Wang, 2009), constraints on pore fluid overpressures and effective stresses based on the analysis of seismic p-wave to s-wave velocity ratios (e.g., Moreno et al., 2014; Tsuji et al., 2014), field-observations from exhumed megathrusts faults (e.g., Angiboust et al., 2015; Cerchiari et al., 2020; Oncken et al., 2022), and analysis of the energy budget of megathrust earthquakes (e.g., Lambert et al., 2021). We therefore expect that near-neutral stress conditions as inferred for Japan and Chile are common along subduction zones worldwide, which implies that most forearcs are prone to failure.

Another factor that controls failure in the forearc is the strength of faults. Coulomb failure stress models usually only describe whether a stress change promotes or inhibits failure, but do not determine the conditions that eventually allow failure, such as the critical pore fluid pressure. Likewise, our models do not describe the conditions for failure, but the total stresses in our models indicate that faults at failure must be almost as weak as the megathrust (cf. Dielforder et al., 2023; Wang et al., 2019; Wang and Hu, 2006; Yang et al., 2013). The low strength may be explained by high pore fluid overpressures ($\lambda > 0.9$) reducing the effective stresses in the forearc or a low intrinsic strength of the fault zone. The latter may be caused by the presence of sheet silicates and the development of shear fabrics in the fault zone, which can reduce the coefficient of friction to values as low as ~0.2 (Ikari and Kopf, 2017; Moore & Lockner, 2004; Tesei et al., 2012).

The requirement of weak faults for failure also implies that their absence may cause tectonic quiescence even though the Coulomb failure stress increases. High pore fluid overpressures may be difficult to sustain through time and over large areas

such that only small fractions of the forearc lithosphere may be close to failure. Stress changes caused by megathrust earthquakes may therefore preferentially drive small earthquakes (Wang et al., 2019). Consistently, the vast majority of the earthquakes investigated in this study have low magnitudes of about 2.5-3.5 and record local failure on small faults. However, the aftershock seismicity of both mainshocks also included damaging earthquakes with magnitudes of 6.6-7.0 inland Japan near Iwaki (Fig. 5a) and in the coastal region near Pichilemu, Chile (Fig. 6a). The large magnitude aftershocks occurred in earthquake clusters affecting the entire crust down to 20 km (Iwaki) and 35 km (Pichilemu) depth, which shows that megathrust earthquakes can cause pervasive failure in the interior of forearcs.

5.2 Robustness of the modelled Coulomb failure stress changes

The modelling results are subject to uncertainties in model parameters like the choice of slip model and coefficient of friction (e.g., Ishibe et al., 2017; Reasenberg and Simpson, 1992; Toda et al., 2011b). Uncertainties in megathrust stress drop may be large, if the earthquake-slip model used for the stress-drop calculation is constrained by onshore geodetic observations only as for the Maule earthquake (Luttrell et al., 2011; Stressler and Barnhart, 2017). There is also a large number of competing slip models for the Tohoku-Oki and Maule earthquakes, as well as models that average different slip model (e.g., Benavente and Cummins, 2013; Delouis et al., 2010; Hooper et al., 2013; Kubota et al., 2022; Minson et al., 2014; Moreno et al., 2012; Sun et al., 2017; Wang et al., 2019; 2020; Wei et al., 2012; Yue et al., 2014). We therefore conducted supplementary finite-element models for the Sendai and Pichilemu cross sections using different stress-drop models (Fig. 11). For Sendai, we used the stress drop-model of Kubota et al. (2022) for the slip model of the same authors. The slip model of Kubota et al. (2022) includes a lower slip (~53 m) near the trench than the slip model of Iinuma et al. (2012) (~80 m), and is similar to the model of Sun et al. (2017) that quantifies the slip near the trench from high-resolution bathymetry differences before and after the Tohoku-Oki earthquake. For the Pichilemu cross section, we used the stress-drop model of Wang et al. (2020) for the average slip model of the same authors, averaging 12 published slip models.

The stress-drop models of Kubota et al. (2022) and Wang et al. (2020) yield smaller stress drops than the models of Brown et al. (2015) and Luttrell et al. (2011) (Fig. 11d). The absolute Coulomb failure stress changes are therefore up to 10 MPa smaller than in the main model results (Figs. 7e, 8e). However, the general patterns of Coulomb failure stress change are similar, while the proportions of aftershocks in areas of positive ΔCFS increase slightly (Figs. 10, 11; Table 1).

The effect of the stress-drop model on the spatial distribution of positive and negative Coulomb failure stress changes is comparatively small, mainly because our modelling approach requires that the post-earthquake stress state is consistent with the fault kinematics of upper-plate aftershocks. The post-earthquake stress state is therefore the same for the different slip models, while the pre-earthquake stress state differs. In detail, the lower stress-drops in the models of Kubota et al. (2022) and Wang et al. (2020) would necessitate that the pre-earthquake stress states are less compressive so that larger forearc areas experience deviatoric tension. The pre-earthquake stress states obtained for the alternative stress-drop models may underestimate the compression of the forearc, at least for Sendai where there is evidence for thrust faulting in the forearc in 100-150 km from the trench before the Tohoku-Oki earthquake (e.g., Nakamura et al., 2016). The mismatch could be

25

removed by increasing the $\mu'_{b\text{-pre}}$ values of the megathrust above the Moho intersection by ~0.006, which translates to an increase in stress drop of about 2 MPa on the shallow megathrust.

For comparison, if the post-earthquake stress state is not constrained to be consistent with the upper-plate fault-kinematics, the Coulomb failure stress change differs significantly. For example, increasing the $\mu'_{b\text{-pre}}$ and $\mu'_{b\text{-post}}$ values in the models by 0.01 causes that the post-earthquake stress states become partially incompatible with the fault kinematics, so that normal faulting occurs in areas of deviatoric compression (Figs. S5-S7 in Supplement). In that case the areas of positive ΔCFS_{opt} become significantly smaller and include only 10–35 % of the aftershocks (Table 1).

We further evaluated the effect of the coefficient of friction μ, the rigidity contrast between the crust and mantle, and of topographic stress on the modelling results. Using a μ value of 0.2 instead of 0.7, slightly reduces the proportions of aftershocks in areas of positive ΔCFS_{opt} (Table 1), but does not change the general pattern of the Coulomb failure stress change (Fig. S8 in Supplement). Removing the rigidity contrast between the crust and the mantle by applying the same Young's modulus of 60 GPa to both, reduces the contrast in total stresses and Coulomb failure stresses at the crust-mantle transition (Figs. S9-S11 in Supplement). The areas of positive ΔCFS_{opt} change slightly and contain less of the aftershocks (Table 1). To test the effect of topographic tresses, we constructed additional models without water loads and a flat surface such that there is no gradient in potential energy and no topographic stresses (Figs. S12-S14 in Supplement). Without topographic stress, the Coulomb failure stress change decreases almost everywhere in the forearc, except for some smaller areas, in which the compression of the forearc increases. The areas of ΔCFS_{opt} contain 0-20 % of the aftershocks (Table 1).

Taken together, we find that the model results vary with the stress-drop model, coefficient of friction and Young's modulus, but are most sensitive to the forearc topography and the forearc stress state after the earthquake. Thus, a robust estimate of the Coulomb failure stress change requires that the topography and stress state are constrained in addition to the megathrust stress drop, as in our models for Japan and Pichilemu, Chile. For comparison, the stress state along the Concepción cross section is less well constrained and the model results are less robust.
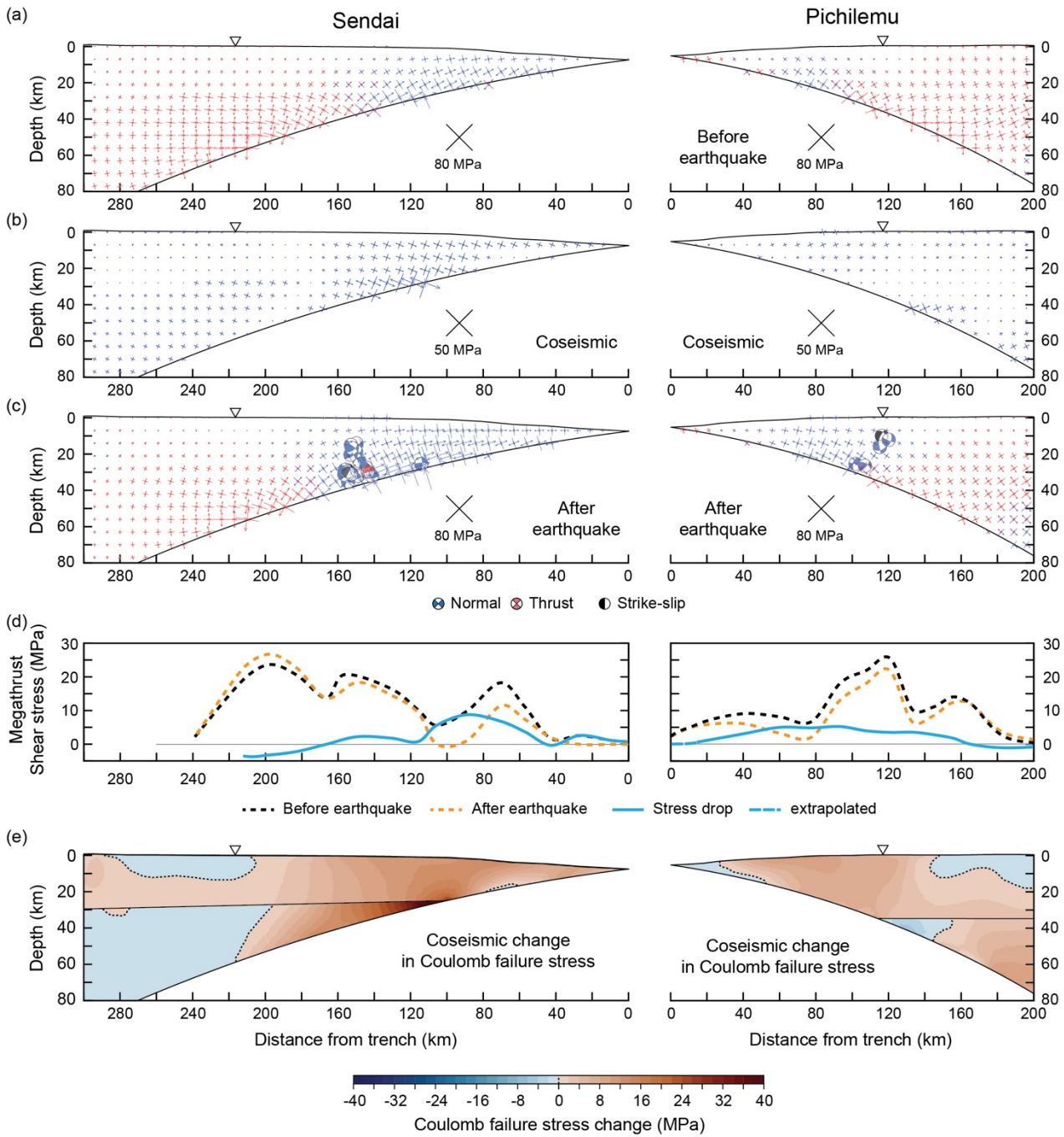
Figure 11: Supplementary Coulomb failure stress models for the Sendai cross section, Japan, using the stress-drop model of Kubota et al. (2022) (left) and the Pichilemu cross section, Chile, using the stress drop model of Wang et al. (2020) (right). The meaning of panels (a-e) is the same as in Fig. 7. The coseismic change in Coulomb failure stress in (e) is calculated for $\mu = 0.7$.

Table 1: Percentages of aftershocks in areas of positive Coulomb failure stress change

Model	Sendai	Iwaki	Pichilemu	Concepcíon
Main[a]	96.7	98.1	87.2	63.5
K22, W20[b]	99.8	–	89.2	–
$\mu'_b + 0.01$[c]	34.9	10.2	26.5	22.5
$\mu = 0.2$[d]	89.1	94.3	67.7	12.6
$E_c = E_m = 60$ GPa[e]	83.8	94.3	86.8	74.4
No topography[f]	0.0	18.6	0.0	10.4

[a]Main results for the stress drop models of Brown et al. (2015) for Japan and Luttrell et al. (2011) for Chile as presented in Figs. 7-9.

[b]Supplementary model results for the stress drop models of Kubota et al. (2022) for Sendai and Wang et al. (2020) for Pichilemu as presented in Fig. 11.

[c]As [a], but for effective coefficients of megathrust friction μ'_b increased by 0.01. See Figs. S5-S7 for details.

[d]As [a], but using a coefficient of friction μ of 0.2 instead of 0.7 for the calculation of the Coulomb failure stress change. See Fig. S8 for details.

[e]As [a], but using the same Young's Modulus of 60 GPa for the crust (E_c) and mantle (E_m). See Figs. S9-S11 for details.

[f]As [a], but without topography and water loads. See Figs. S12-S14 for details.

5.3 Significance of the modelled stress changes as triggers of aftershock seismicity

The finite element models indicate that the megathrust stress drop during the Tohoku-Oki and Maule earthquakes caused a broad increase in Coulomb failure stress in the forearc, so that the majority of all the forearc seismicity occurred in areas of Coulomb failure stress increase (Fig. 10). For Japan, there is a continuous record of forearc seismicity covering the time before and after the Tohoku-Oki earthquake (Japan Meteorological Agency). The forearc seismicity along the investigated cross sections occurred immediately after the earthquake and throughout the forearc (Figs. S3 and S4 in Supplement) (e.g., Dielforder et al., 2023; Hasegawa et al., 2012; Toda et al., 2011a; Yoshida et al., 2012). Seismicity rates were highest in the month following the Tohoku earthquake and decayed at a power-law like rate afterwards. For Chile, a detailed record is available only for the time about 2 weeks after the Maule earthquake (Lange et al., 2012, Şen et al., 2015), but the record also shows a decrease in seismicity rates, similar as for Japan (Fig. S3 in Supplement). Overall, the records for Japan and Chile indicate that the forearc seismicity is related to the mainshock and our modelling results indicate that most of the seismicity was promoted and likely triggered by the stress drop on the megathrust.

We further showed that the investigated Coulomb failure stress change depends on the superposition of topographic and tectonic stresses and that increases in ΔCFS_{opt} require a prevalence of topographic stress after the earthquake. The dataset shows different characteristics that corroborate the influence of topography on aftershock triggering. The aftershock seismicity is dominated by normal faulting, which requires deviatoric tension. The tension resulting from forearc topography

agrees well with spatial extent of normal faulting, but also allows deviatoric compression in areas of thrust faulting like inland Japan. The modelling results further indicate that all of the aftershock seismicity was coupled to a rotation of σ_1 toward the vertical and partially involved an increase in differential stress (~84 % and ~11 % of the aftershocks in Japan and Chile, respectively). For Coulomb failure, the strength of faults, i.e., the stress at failure, decreases with increasing plunge of σ_1, while increases in differential stress generally promote failure. Both the modelled stress rotation and the increases in differential stress result from the effect of topography and explain the triggering of aftershocks.

The modelled Coulomb failure stress changes also reveal some details resulting from topography that appear to influence the distribution of seismicity. The Sendai models show seaward-inclined isolines of ΔCFS_{opt} (Fig. 10), which is primarily due to the submarine margin relief. The landward extent of seismicity in the lower crust and mantle at about 160–200 km from the trench follows these isolines (Figs. 7e, 11). The Sendai models further show an increase in Coulomb failure stress in 200-280 km distance only in the lower crust, while the Iwaki model shows an increase also in the upper crust. The difference is partially due to a local topographic high along the coast of Iwaki (the Abukuma plateau), which is missing near Sendai. For Pichilemu, isolines of ΔCFS_{opt} in 80–130 km distance form landward-inclined lobes that encompass the main cluster of seismicity that is landward-inclined too (Fig. 8e). The landward inclination is due to the topography of the Chilean Central Valley, which forms a gentle depression between the Coastal Range and the high Andes. Likewise, the decrease in Coulomb failure stress in the crust in 130-200 km distance results from the valley.

The consistency in the aftershock-ΔCFS patterns does, however, not imply that there is a general, simple dependence of the seismicity distribution on the earthquake stress changes. For example, the largest earthquake slip and the largest stress changes in Japan occurred near the Tohoku-Oki hypocentre along the Sendai cross section, but most of the aftershocks occurred ~140 km to the southwest in the coastal area near Iwaki, where the earthquake slip and stress changes were comparatively low (Figs. 5, 7 and 8). For comparison, in Chile, the largest earthquake slip and stress changes occurred near Pichilemu, ~200 km north of the mainshock hypocentre, where also most of the aftershock seismicity occurred (Figs. 6 and 9).

The differences in the aftershock occurrence likely reflect spatial heterogeneities in fault strength and proximity to failure. For Japan, our model results indicate that tectonically active forearc areas along the Iwaki cross section where in a near-neutral stress state already before the Tohoku-Oki earthquake (Fig. 8a), which is consistent with mixed upper-plate fault kinematic near Iwaki in the years before the Tohoku-Oki earthquake (Hasegawa et al., 2012; Nakamura et al., 2016). Thus, normal faults along the Iwaki transect were closer to failure than normal faults along the Sendai transect that experienced deviatoric compression before the mainshock (Fig. 7a) (Wang et al., 2019). The comparatively small stress changes near Iwaki may thus have been enough to trigger normal faulting.

For comparison, the outer forearc along Sendai transect at <140 km from the trench shows comparatively little seismicity despite large increases in Coulomb failure stress (Fig. 7). The outer forearc experienced strong coseismic dilation due to the

large slip near the trench causing seaward surface displacements ≥20m (Kido et al., 2011; Sato et al., 2011), which may have caused dilatant hardening (e.g., Brace, 1978), i.e., a drop in pore fluid pressure and respective increase in fault strength.

630 The aftershock seismicity of the Tohoku-Oki and Maule earthquakes may have been further affected by processes not captured in our models. For example, aftershocks can be triggered by dynamic stress changes resulting from the passage of seismic waves emitted by the mainshock (e.g., Gomberg et al., 2004; Kato et al., 2013; Miyazawa, 2011). Coulomb failure stress changes caused by seismic waves can reach a few MPa near the earthquake hypocentre (e.g., Kilb et al., 2000; Miyazawa, 2011), which is comparable to the Coulomb failure stress change caused by the stress drop on the megathrust.

635 Dynamic triggering in the nearfield of the earthquake should be quasi-instantaneous with the mainshock (e.g., Belardinelli et al., 2003; Harris, 1998) and may have affected the immediate seismic response to the Tohoku-Oki and Maule earthquakes. The longer-term aftershock seismicity may have been influenced by poroelastic effects and pore pressure changes (e.g., Cocco and Rice, 2002; Hainzl, 2004; Peikert et al., 2024; Peña et al., 2022; Terakawa et al., 2013; Yoshida et al., 2017), viscoelastic stress relaxation in the mantle wedge and lower crust (Bagge and Hampel, 2017; Becker et al., 2018; Diao et al.,

640 2014; Sun et al., 2014), and stress changes induced by larger aftershocks (M_w ≥5), as they occurred for example near Iwaki and Pichilemu (e.g., Fukushima et al., 2013; 2018; Lange et al., 2012; Ryder et al., 2012; Wimpenny et al., 2023).

5.4 Comparison with previous Coulomb failure stress models

The results of the finite-element models indicate that the majority of the aftershock seismicity along the studied forearc cross sections occurred in areas of Coulomb failure stress increase (~97-98 % for Japan, ~87 % and ~64 % for Pichilemu and

645 Concepción, respectively) (Table 1). The proportions of positively stressed aftershocks (i.e., aftershocks in areas of positive ΔCFS) are higher than in previous Coulomb failure stress models based on dislocation solutions for a fault embedded in an elastic half-space. Toda et al. (2011b) investigated normal faulting events in the Japanese forearc after the Tohoku-Oki and found that ~71 % of them were positively stressed. Ishibe et al. (2017) found that ~60 % and ~43 % of the aftershocks of the Tohoku-Oki earthquake and Maule earthquake, respectively, were positively stressed. Miao and Zhu (2012) concluded that

650 less than 50 % of the aftershock seismicity of the Tohoku-Oki and Maule earthquake was positively stressed. It is important to note that the above studies used different approaches and datasets, which makes a direct comparison of model results difficult. For example, the studies investigate larger areas than we do and partially include lower plate and interplate events in the analysis.

Toda et al. (2011b) and Ishibe et al. (2017) resolved the Coulomb failure stress on nodal planes of earthquake focal

655 mechanisms, i.e., the authors determined the Coulomb failure stress change on specified failure planes (equation (5)). The analytical stress solutions presented in section 2 show that the sign of ΔCFS$_{sf}$ and ΔCFS$_{opt}$ values should match if the investigated type of faulting agrees with the mechanical state (e.g., normal faulting under deviatoric tension) (Fig. 4). Consistently, the results of Toda et al. (2011b), Ishibe et al. (2017), and our study indicate an increase in Coulomb failure stress in forearc areas experiencing normal faulting, for example, near Iwaki, Japan, and Pichilemu, Chile. However, there

660 are also significant differences in the modelling result. For example, Ishibe et al. (2017) find that the slip model of Luttrell et

al. (2011) for the Maule earthquake yields a mean decrease in Coulomb failure stress, while we find that the model causes broad increases in Coulomb failure stress that explain the aftershock seismicity well. Toda et al. (2011a) resolved the Coulomb failure stress change on the nodal planes of earthquakes from before the Tohoku-Oki earthquake and compared it with changes in seismicity rate. If the regional stress field does not change much during the mainshock, the earthquake stress change may trigger faults that have been active before the mainshock. However, the approach may be misleading if the regional stress field changes. The authors therefore exclude the area near Iwaki from their analysis, even though the area records the most intense change in seismicity rate and the most severe aftershocks. For comparison, our approach takes into account changes in the regional stress and the ΔCFS_{opt} can be directly compared with seismicity rate changes without resolving the stress change on pre-mainshock nodal planes. The Coulomb failure stress model of Terakawa et al. (2013) yields a decrease in Coulomb failure stress inland Japan and offshore Sendai, such that large portions of the aftershock seismicity are negatively stressed. The authors argue that the negatively stressed aftershocks may record a triggering of misoriented faults due to increases in pore fluid pressure. For comparison, our models indicate that the seismicity offshore Sendai as well as near the volcanic arc inland Japan was positively stressed and does not require a complex triggering mechanism.

Finally, the analytical stress solutions and the finite-element models yield ΔCFS values that can reach 10s of MPa, which is similar to the magnitude of the modelled differential stress and changes in differential stress (Figs. 3, 7-9), and distinctly higher than previous estimates of ΔCFS on the order of 0.01–1 MPa (e.g., Farías et al., 2011; Ishibe et al., 2017; Jara-Munoz et al., 2022; Nakamura et al., 2016; Ryder et al., 2012; Stressler and Barnhart, 2017; Terakawa et al., 2013; Toda et al., 2011a, 2011b; Qiu and Chan, 2019). The ΔCFS values increase with the megathrust stress drop and are particularly high if the stress state switches from deviatoric compression to deviatoric tension, especially in the proximity of steep margin topography. Accordingly, we find that the largest Coulomb failure stress changes occur along the Sendai transect, Japan, and the Pichilemu transect, Chile, close to the shelf break at about 100 km distance from the trench (Figs. 7 and 9). In comparison, the Coulomb failure stress changes are lower along the Iwaki transect, Japan, and the Concepción transect, Chile, were the megathrust stress drop and the stress changes in the forearc are smaller (Fig. 8 and 9).

6 Conclusions

Our analysis illustrates that topographic stress allows the stress state in a forearc to switch from deviatoric compression to deviatoric tension, if the shear stress on the megathrust is sufficiently low. The switch in stress state is the main factor that promotes widespread aftershock seismicity at the scale of the forearc. Without the stress reversal, megathrust earthquakes have the tendency to stabilize the forearc and inhibit aftershock seismicity. A switch in stress state is supported if the megathrust is very weak and the forearc is close to a neutral state (margin normal compression ≈ margin normal tension) before the earthquake. Near-neutral stress conditions have been inferred for most global subduction zones (Dielforder et al.,

2020; Heuret et al., 2011; Lamb, 2006). Thus, the mechanisms evaluated here are crucial for assessing the geohazard at convergent margins.

The dependence of the forearc stability on the stress state can be taken into account by calculating the Coulomb failure stress change as difference in Coulomb failure stress between the optimal failure planes before and after the earthquake, ΔCFS_{opt}, but this requires to constrain the total stresses in the forearc. We show that the total stresses may be constrained within reasonable uncertainties by moment tensor solutions of upper-plate earthquakes and estimates of the megathrust stress drop in the mainshock. Thus, the availability of earthquake moment tensor solutions and stress drop estimates is crucial for evaluating seismic hazards at active margins. This underlines the importance of installing high-quality geophysical networks, such as those in Japan. If detailed geophysical observations are not available, ΔCFS_{opt} may still be estimated, for example by using for the stress calculations an effective coefficient of friction for the megathrust determined by other means. However, this approach can introduce uncertainties and lead to less accurate models, as likely reflected in our model for the Concepción cross section in Chile.

The benefit of constraining the total stresses before and after the earthquake is that it allows a better estimate of Coulomb failure stress changes and provides insights into the factors promoting aftershock seismicity. Our models for Japan reveal differences in the preseismic stress conditions along the Sendai and Iwaki cross sections, which may explain why the comparatively small stress changes near Iwaki could trigger intense aftershock seismicity. In contrast, the intense aftershock seismicity near Pichilemu (Chile) was dependent on the large stress changes that resulted from large slip and stress drop on the megathrust ~200 km north of the mainshock hypocentre. We further find that the aftershock occurrence including the large magnitude events near Iwaki, Japan, and Pichilemu, Chile, was influenced by the local forearc topography. Our findings therefore reveal that topography is not only a prerequisite for widespread aftershock seismicity but also influences its details.

Finally, our models illustrate the importance of forearc mechanics for understanding Coulomb failure stress changes and aftershock triggering, but they are currently limited in their application to two-dimensional cross sections normal to the plate margin. Future work will therefore include the development of three-dimensional models, which will account for differences in continental-margin relief and total stresses along strike of the margin.

Appendix A

The stress solutions for an elastic-perfectly Coulomb plastic wedge can be written in terms of effective stresses as (Wang and Hu, 2006)

$$\bar{\sigma}_x = m(1-\lambda)\rho gz \cos\alpha \tag{A1a}$$

$$\bar{\sigma}_z = (1-\lambda)\rho gz \cos\alpha \tag{A1b}$$

$$\tau_{xz} = (1-\rho')\rho gz \sin\alpha \tag{A1c}$$

where

$$m = 1 + \frac{2[\tan\alpha' + \mu'_b/(1-\lambda)]}{\sin 2\theta[1 - \mu'_b/(1-\lambda)\tan\theta]} - \frac{2\tan\alpha'}{\tan\theta} \tag{A2}$$

725 and

$$\tan\alpha' = \frac{1-\rho'}{1-\lambda}\tan\alpha \tag{A3}$$

with $\theta = \alpha + \beta$, and $\rho' = \rho_w/\rho$. The total stresses σ_x and σ_z can be obtained by solving equation (A1) for $\lambda = 0$.

The principal stresses can be written as

$$\sigma_1 = \sigma_x \cos^2\psi_0 + \sigma_z \sin^2\psi_0 + 2\tau_{xy}\sin\psi_0\cos\psi_0 \tag{A4a}$$

730
$$\sigma_3 = \sigma_x \sin^2\psi_0 + \sigma_z \cos^2\psi_0 - 2\tau_{xy}\sin\psi_0\cos\psi_0 \tag{A4b}$$

where ψ_0 is the angle between the surface of the wedge and the axis of σ_1 (Fig. 1b). Angle ψ_0 is determined from the following equation (Wang and Hu, 2006)

$$\frac{\tan 2\psi_0}{\cos\varphi^p \sec 2\psi_0 - 1} = \frac{\tan\alpha'}{1+\eta} \tag{A5}$$

where

735
$$\varphi^p = \arcsin\sqrt{\frac{(m-1)^2 + 4\tan^2\alpha'}{(2\eta + m + 1)^2}} \tag{A6}$$

The cohesion gradient η is a dimensionless constant that allows to account for wedge cohesion (Zhao et al., 1986). Equation (A5) may be rewritten in explicit forms as

$$\psi_0 = \frac{1}{2}\left(\arcsin\left(\frac{\sin\alpha''}{\sin\varphi^p}\right) - \alpha''\right), \; \psi_0 \leq \pi/4 - \alpha''/2 \tag{A7a}$$

$$\psi_0 = \frac{\pi}{2} + \frac{1}{2}\left(\arcsin\left(\frac{\sin\alpha''}{-\sin\varphi^p}\right) - \alpha''\right), \; \psi_0 > \pi/4 - \alpha''/2 \tag{A7b}$$

740 where

$$\alpha'' = \arctan\left(\frac{\tan\alpha'}{1+\eta}\right) \tag{A8}$$

The wedge enters a critical state if

$$m = m^c = 1 + \frac{2(1+\eta)}{\csc\varphi\sec 2\psi_0^c - 1} \tag{A9}$$

where $\varphi = \arctan\mu$ and ψ_0^c is the angle of between the axis of σ_1 and the surface slope at critical state (Wang and Hu, 2006,

745 Zhao et al., 1986). Angle ψ_0^c is determined from the following equation similar to Equation (A5)

$$\frac{\tan 2\psi_0^c}{\cos\varphi\sec 2\psi_0^c - 1} = \frac{\tan\alpha'}{1+\eta} \tag{A10}$$

The effective coefficient of megathrust friction at neutral stress state can be calculated as (Wang and Hu, 2006)

$$\mu'_{b-N} = \frac{(1-\lambda)\cos 2\theta}{\cot\alpha' + \sin\theta} \tag{A11}$$

750 *Code availability:* The finite-element models were calculated, processed, and plotted using the commercial software packages ABAQUS (Abaqus, 2014), MATLAB (The MathWorks Inc., 2022) and the Matlab tool Abaqus2Matlab by

Papazafeiropoulos et al. (2017). The maps in Fig. 7 and 8 were produced with GMT (Wessel et al., 2019). Colour schemes follow 'Scientific colour maps' (Crameri et al., 2020).

References

ABAQUS: Analysis User's Manual, Version 6.14. Dassault Systems Simulia, Inc., http://62.108.178.35:2080/v6.14/index.html , 2014

Allmann, B. P., and Shearer, P. M.: Global variations of stress drop for moderate to large earthquakes, J. Geophys. Res., 114, 770 B01310, https://doi.org/10.1029/2008JB005821, 2009.

Amante, C., and Eakins, B. W.: ETOPO1 1 Arc-Minute Global Relief model, NOAA Technical Memorandum. https://doi.org/10.7289/V5C8276M, 2009.

Angiboust, S., Kirsch, J., Oncken, O., Glodny, J., Monié, P., and Rybacki, E.: Probing the transition between seismically coupled and decoupled segments along an ancient subduction interface, Geochem., Geophys., Geosys., 16, 1905–1922. 775 https://doi.org/10.1002/2015GC005776, 2015.

Asano, Y., Saito, T., Ito, Y., Shiomi, K., Hirose, H., Matsumoto, T., Aoi, S., Hori, S., and Sekiguchi, S.: Spatial distribution and focal mechanisms of aftershocks of the 2011 off the Pacific coast of Tohoku Earthquake, Earth Planets Space, 63, 669–673. https://doi.org/10.5047/eps.2011.06.016, 2011.

Bagge, M., and Hampel, A.: Three-dimensional finite-element modelling of coseismic Coulomb stress changes on intra-780 continental dip-slip faults, Tectonophysics, 684, 52–62. https://doi.org/10.1016/j.tecto.2015.10.006, 2016.

Bagge, M., and Hampel, A.: Postseismic Coulomb stress changes on intra-continental dip-slip faults due to viscoelastic relaxation in the lower crust and lithospheric mantle: insights from 3D finite-element modelling, Int. J. Earth Sci., 106, 2895–2914. https://doi.org/10.1007/s00531-017-1467-8, 2017.

Bagge, M., Hampel, A., and Gold, R. D.: Modeling the Holocene slip history of the Wasatch fault (Utah): Coseismic and

785   postseismic Coulomb stress changes and implications ofr paleoseismcity and seismic hazard, Geol. Soc. Am. Bull., 131, 43–57, https://doi.org/10.1130/B31906.1, 2018.

Becker, T. W., Hashima, A., Freed, Am. M., and Sato, H.: Stress change before and after the 2011 M9 Tohoku-Oki earthquake. Earth Planet. Sci. Lett., 504, 174–184, https://doi.org/10.1016/j.epsl.2018.09.035, 2018.

Bedford, J., Moreno, M., Li, S., Oncken, O., Baez, J. C., Bevis, M., Heidbach, O., and Lange, D.,: Separating rapid

790   relocking, afterslip, and viscoelastic relaxation: An application of the postseismic straightening method to the Maule 2010 cGPS. J. Geophys. Res., 121, 7618–7638, https://doi.org/10.1002/2016JB013093, 2016.

Belardinelli, M. E., Bizzarri, A., and Cocco, M: Earthquake triggering by static and dynamic stress changes. J. Geophys. Res., 108, 2135, https://doi.org/10.1029/2002JB001779, 2003.

Benavente, R., and Cummins, P. R.: Simple and reliable finite fault solutions for large earthquakes using the W-phase: The

795   Maule (Mw = 8.8) and Tohoku (Mw = 9.0) earthquakes, Geophys. Res. Lett., 40, 3591–3595, https://doi.org/10.1002/grl.50648, 2013.

Bilek, S. L., and Lay, T.: Tsunami earthquakes possibly widespread manifestations of frictional conditional stability, Geophys. Res. Lett., 29, 1673, https://doi.org/10.1029/2002GL015215, 2002.

Bird, P.: Stress and temperature in subduction shear zones: Tonga and Mariana, Geophys. J. Int., 55, 411–434,

800   https://doi.org/10.1111/j.1365-246X.1978.tb04280.x, 1978.

Brace, W. F.: Volume changes during fracture and frictional sliding: A review, Pageoph, 116, 603–614, 1978.

Brodsky, E. E., Mori, J. J., Anderson, L., Chester, F. M., Conin, M., Dunham, E. M., Eguchi, N., Fulton, P. M., Hino, R., Hirose, T., Ikai, M. J., Ishikawa, T., Jeppson, T., Kano, Y., Kirkpatrick, J., Kodaira, S., Lin, W., Nakamura, Y., Rabinowitz, H. S., Regalla, C., Remitti, F., Rowe, C., Saffer, D. M., Saito, S., Sample, J., Sanada, Y., Savage, H. M., Sun, T., Toczko, S.,

805   Ujiie, K., Wolfson-Schwehr, M., and Yang, T.: The state of stress on the fault before, during, and after a major earthquake, Annu. Rev. Earth Planet. Sci., 48, 49–74, https://doi.org/10.1146/annurev-earth-053018-060507, 2020.

Brown, L., Wang, K., and Sun, T.: Static stress drop in the M_w 9 Tohoku-oki earthquake: Heterogeneous distribution and low average value, Geophys. Res. Lett., 42, 10,595–10,600, https://doi.org/10.1002/2015GL066361, 2015.

Calle-Gardella, D., Comte, D., Farías, M., Roecker, S., and Rietbrock, A.: Three-dimensional local earthquake tomography

810   of pre-Cenozoic structures in the coastal margin of central Chile: Pichilemu fault system, *J. Seismol.*, 25, 521–533, https://doi.org/10.1007/s10950-021-09989-w, 2021.

Cerchiari, A., Remitti, F., Mittempergher, S., Festa, A., Lugli, F., and Cipriani, A.: Cyclical variations of fluid sources and stress state in a shallow megathrust-zone mélange, J. Geol. Soc., 177, 647–659. https://doi.org/10.1144/jgs2019-072, 2020.

Chiba, K., Iio, Y., and Fukahata, Y.: Detailed stress fields in the focal region of the 2011 off the Pacific coast of Tohoku

815   Earthquake–Implication for the distribution of moment release–, Earth Planets Space, 64, 1157–1165. https://doi.org/10.5047/eps.2012.07.008, 2013.

Cocco, M., and Rice, J. R.: Pore pressure and poroelasticity effects in Coulomb stress analysis of earthquake interactions, J. Geophys. Res., 107, 2030, https://doi.org/10.1029/2000JB000138, 2002.

Cubas, N., Avouac, J.-P., Leroy, Y. M., and Pons, A.: Low friction along the high slip patch of the 2011 M_w 9.0 Tohoku-Oki earthquake required from the wedge structure and extensional splay faults, Geophys. Res. Lett., 40, 4231–4237, https://doi.org/10.1002/grl.50682, 2013.

Crameri, F., Shephard, G. E. and Heron P. J.: The misuse of colour in science communication, Nat. Commun, 11, 5444, https://doi.org/10.1038/s41467-020-19160-7, 2020.

Dahlen, F. A.: Noncohesive critical Coulomb wedges: An exact solution, J. Geophys. Res., 89, 10,125– 10,133, 1984.

Dahlen, F. A.: Critical taper model of fold-and-thrust belts and accretionary wedges, Annu. Rev. Earth Planet. Sci., 18, 55–99, 1990.

Delouis, B., Nocquet, J. M., and Vallée, M.: Slip distribution of the February 27, 2010 Mw = 8.8 Maule earthquake, Central Chile, from static and high-rate GPS, InSAR, and broadband teleseismic data, Geophys. Res. Lett., 37, L17305, https://doi.org/10.1029/2010GL043899, 2010.

Dewey, J. W., Choy, G., Presgrave, B., Sipkin, S., Tarr, A. C., Benz, H., Earle, P., and Wald, D.: Seismicity associated with the Sumatra–Andaman Islands earthquake of 26 December 2004, Bull. Seismol. Soc. Am., 97, S25–S42, https://doi.org/10.1785/0120050626, 2007.

Diao, F., Xiong, X., Wang, R., Zheng, Y., Walter, T. R., Weng, H., & Li, J.: Overlapping post-seismic deformation processes: Afterslip and viscoelastic relaxation following the 2011 Mw 9.0 Tohoku (Japan) earthquake, Geophys. J. Int., 196, 218–229, https://doi.org/10.1093/gji/ggt376, 2014.

Dielforder, A.: Constraining the strength of megathrusts from fault geometries and application to the Alpine collision zone, Earth Planet. Sci. Lett., 474, 49–58, https://doi.org/10.1016/j.epsl.2017.06.021, 2017.

Dielforder, A., and Hampel, A.: Force-balance analysis of stress changes during the subduction-collision transition and implications for the rise of mountain belts, J. Geophys. Res., 126, e2020JB020914, https://doi. org/10.1029/2020JB020914, 2021.

Dielforder, A., Bocchini, G. M., Kemna, K., Hampel, A., Harrington, R. M., and Oncken, O.: Megathrust stress drop as trigger of aftershock seismicity: Insights from the 2011 Tohoku earthquake, Japan, Geophys. Res. Lett., 50, e2022GL101320, https://doi.org/10.1029/2022GL101320, 2023.

Dielforder, A., Hetzel, R., and Oncken, O.: Megathrust shear force controls mountain height at convergent plate margins, Nature, 582, 225–229, https://doi.org/10.1038/s41586-020-2340-7, 2020.

Farías, M., Comte, D., Roecker, S., Carrizo, D. and Pardo, M.: Crustal extensional faulting triggered by the 2010 Chilean earthquake: The Pichilemu Seismic Sequence. Tectonics, 30, TC6010, https://doi.org/10.1029/2011TC002888, 2011.

Freed, A. M., and Lin, J.: Time-dependent changes in failure stress following thrust earthquakes, J. Geophys. Res., 103, 24393–24409, https://doi.org/10.1029/98JB01764, 1998.

850   Fukushima, Y., Takada, Y., and Hashimoto, M.: Complex ruptures of the 11 April 2011 M_w 6.6 Iwaki earthquake triggered by the 11 March 2011 Mw 9.0 Tohoku earthquake, Japan, Bull. Seismol. Soc. Am., 103, 1572–1583, https://doi.org/10.1785/0120120140 , 2013.

Fukushima, Y., Toda, S., Miura, S., Ishimura, D., Fukuda, J., Demachi, T., and Tachibana, K.: Extremely early recurrence of intraplate fault rupture following the Tohoku-Oki earthquake, Nat. Geosci., 11, 777–781, https://doi.org/10.1038/s41561-855   018-0201-x, 2018.

Gao, X., and Wang, K.: Strength of stick-slip and creeping subduction megathrusts from heat flow observations, *Science*, 345, 1038–1041, https://doi.org/10.1126/science.1255487, 2014.

Gomberg, J., Bodin, P., Larson, K., and Dragert, H.: Earthquake nucleation by transient deformations caused by the M = 7.9 Denali, Alaska, earthquake, *Nature*, 427, 621–624, https://doi.org/10.1038/nature02335, 2004.

860   Hainzl, S.: Seismicity patterns of earthquake swarms due to fluid intrusion and stress triggering, Geophys. J. Int., 159, 1090–1096, https://doi.org/10.1111/j.1365-246X.2004.02463.X, 2004.

Hardebeck, J. L.: Coseismic and postseismic stress rotations due to great subduction zone earthquakes, Geophys. Res. Lett., *39*, L21313, https://doi.org/10.1029/2012GL053438, 2012.

Hardebeck, J. L.: The impact of static stress change, dynamic stress change, and the background stress on aftershock focal 865   mechanisms, J. Geophys., Res., 119, 8239–8266, https//doi.org/10.1002/2014JB011533, 2014.

Hardebeck, J. L., Nazareth, J. J., and Hauksson, E.: The static stress change triggering model: Constraints from two Southern California aftershock sequences, J. Geophys. Res., 103, 24,427–24,437, https://doi.org/10.1029/98JB00573, 1998.

Harris, R. A.: Introduction to Special Section: Stress Triggers, Stress Shadows, and Implications for Seismic Hazard, J. Geophys. Res., 103, 24347–24358, https://doi.org/10.1029/98JB01576, 1998.

870   Hasegawa, A., Yoshida, K., Asano, Y., Okada, T., Iinuma, T., and Ito, Y.: Change in stress field after the 2011 great Tohoku-Oki earthquake, Earth Planet. Sci. Lett., 355-356, 231–243, https://doi.org/10.1016/j.epsl.2012.08.042, 2012.

Hasegawa, A., Yoshida, K., and Okada, T.: Nearly complete stress drop in the 2011 M_w 9.0 Tohoku Earthquake, Earth Planets Space, 63, 703–707, https://doi.org/10.5047/eps.2011.06.007, 2011.

Hayes, G. P., Bergman, E., Johnson, K. L., Benz, H. M., Brown, L., and Meltzer, A. S.: Seismotectonic framework of the 875   2010 February 27 M_w 8.8 Maule, Chile earthquake sequence, Geophys. J. Int., 195, 1034–1051. https://doi.org/10.1093/gji/ggt238, 2013.

Hayes, G. P., Moore, G. L., Portner, D. E., Hearne, M., Flamme, H., Furtney, M., and Smoczyk, G. M.: Slab2, A comprehensive subduction zone geometry model, Science, 362, 58–61, https://doi.org/10.1126/science.aat4723, 2018.

Herman, M. W., and Govers, R.: Stress evolution during the megathrust earthquake cycle and its role in triggering 880   extensional deformation in subduction zones, Earth Planet. Sci. Lett., 544, 116379, https:/doi.org/10.1016/j.eepsl.2020.116379, 2020.

Heuret, A., Lallemand, S., Funiciello, F., Piromallo, C., and Faccenna, C.: Physical characteristics of subduction interface type seismogenic zones revisited, Geochem., Geophys., Geosys.*,* 12, Q01004, https://doi.org/10.1029/2010GC003230, 2011.

Hooper, A., Pietrzak, J., Simons, H., Cui, W., Riva, R., Naeije, M., Terwisscha van Scheltinga, A., Schrama, E., Stelling, G., and Socquet, A.: Importance of horizontal seafloor motion on tsunami height for the 2011 Mw = 9.0 Tohoku-Oki earthquake, Earth Planet. Sci. Lett., 361, 469–479, https://doi.org/10.1016/j.epsl.2012.11.013, 2013.

Iinuma, T., Hino, R., Kido, M., Inazu, D., Osada, Y., Ito, M. O., Tsushima, H., Suzuki, S., Fujimoto, H., and Miura, S.: Coseismic slip distribution of the 2011 off the Pacific Coast of Tohoku Earthquake (M9.0) refined by means of seafloor geodetic data, J. Geophys. Res., 117, B07409, https://doi.org/10.1029/2012JB009186, 2012.

Ikari, M. J., and Kopf, A. J.: Seismic potential of weak, near-surface faults revealed at plate tectonic slip rates, Science advances, 3, e1701269, https://doi.org/10.1126/sciadv.1701269, 2017.

Ishibe, T., Ogata, Y., Tsuruoka, H. and Stake, K.: Testing the Coulomb stress triggering hypothesis for three recent megathrust earthquakes, Geosci. Lett., 4:5, https://doi.org/10.1186/s40562-017-0070-y, 2017.

Jara-Muñoz, J., Melnick, D., Li, S., Socquet, A., Cortés-Aranda, J., Brill, D., and Strecker, M. R.: The cryptic seismic potential of the Pichilemu blind fault in Chile revealed by off-fault geomorphology, Nat. Commun., 13, 3371. https://doi.org/10.1038/s41467-022-30754-1, 2022.

Kanamori, H., and Brodsky, E. E.: The physics of earthquakes, Reports on Progress in Physics, 67, 1429–1496. https://doi.org/10.1088/0034-4885/67/8/R03, 2004.

Kato, A., Igarashi, T., Obara, K., Sakai, S., Takeda, T., Saiga, A., Iidaka, T., Iwasakim T., Hirata, N., Goto, K., Miayamachi, H., Matsushima, T., Kubo, A., Katao, H., Yamanaka, Y., Terakawa, T., Nakamichi, H., Okuda, T., Horikawa, S., Tsumura, N., Umino, N., Okada, T., Kosuga, M., Takahashi, H., and Yamada, T.: Imaging the source regions or normal faulting sequences induced by the 2011 M9.0 Tohoku-Oki earthquake, Geophys. Res. Lett., 40, 273–278. https://doi.org/10.1002/grl.50104, 2013.

Kido, M., Osada, Y., Fujimoto, H., Hino, R., and Ito, Y.: Trench-normal variation in observed seafloor displacements associated with the 2011 Tohoku-Oki earthquake, Geophys. Res. Lett., 38, L24303, https://doi.org/10.1029/2011GL050057, 2011.

Kilb, D., Gomberg, J., and Bodin, P.: Triggering of earthquake aftershocks by dynamic stress, Nature, 408, 570–574, https://doi.org/10.1038/35046046, 2000.

King, G. C. P., Stein, R. S., and Lin, J.: Static stress changes and the triggering of earthquakes, Bull. Seismol. Soc. Am., 84, 935–953, https://doi.org/10.1785/BSSA0840030935, 1994.

Kubota, T., Saito, T., and Hino R.: A new mechanical perspective on a shallow megathrust near-trench slip from the high-resolution fault model of the 2011 Tohoku-Oki earthquake, Prog. Earth Planet. Sci., 9, 68, https://doi.org/10.1186/s40645-022-00524-0, 2022.

Lamb, S.: Shear stresses on megathrusts: Implications for mountain building behind subduction zones, J. Geophys. Res., 111, B07401, https://doi.org/10.1029/2005JB003916, 2006.

Lambert, V., Lapusta, N., and Perry, S.: Propagation of large earthquakes as self-healing pulses or mild cracks, Nature, 591, 252–259. https://doi.org/10.1038/s41586-021-03248-1, 2021.

Lange, D., Tilmann, F., Barrientos, S. E., Contreras-Reyes, E., Methe, P., Moreno, M., Heit, B., Agurto, H., Bernard, P., Vilotte, J.-P., and Beck, S.: Aftershock seismicity of the 27 February 2010 M_w 8.8 Maule earthquake rupture zone, Earth Planet. Sci. Lett., 317–318, 413–425, https://doi.org/10.1016/j.epsl.2011.11.034, 2012.

Lee, S. J., B. S. Huang, M. Ando, H. C. Chiu, and Wang, J. H.: Evidence of large scale repeating slip during the 2011 Tohoku-Oki earthquake, Geophys. Res. Lett., 38, L19306, https://doi.org/10.1029/2011GL049580, 2011.

Lin, J., and Stein, R. S.: Stress triggering in thrust and subduction earthquakes and stress interaction between the southern San Andreas and nearby thrust and strike-slip faults, J. Geophys. Res., 109, B02303, https://doi.org/10.1029/2003JB002607, 2004.

Luttrell, K. M., Tong, X:, Sandwell, D. T., Brooks, B. A., and Bevis M. G.: Estimates of stress drop and crustal tectonic stress from the 27 February 2010 Maule, Chile, earthquake: Implications for fault strength, J. Geophys. Res., 116, B11401, https://doi.org/10.1029/2011JB008509, 2011.

Matthies, F., Dielforder, A., and Hampel, A.: Force-balance modelling of the impact of glacial erosion, trench sedimentation, megathrust weakening and glacial loading on the stress state of the crust at active continental margins, Tectonophysics, 871, 230180, https://doi.org/10.1016/j.tecto.2023.230180, 2024.

Miao M., and Zhu S.-B.: A study of the impact of static Coulomb stress changes of megathrust earthquakes along subduction zone on the following aftershocks, Chin. J. Geophys., 55, https://doi.org/10.1002/cjg2.1748, 39–551, 2012.

Minson, S. E., Simons, M., Beck, J. L., Ortega, F., Jiang, J., Owen, S. E., Moore, A. W., Inbal, A., and Sladen, A.: Bayesian inversion for finite fault earthquake source models—II: The 2011 great Tohoku-oki, Japan earthquake, Geophys. J. Int., 198, 922–940., 2014.

Miyazawa, M.: Propagation of an earthquake triggering front from the 2011 Tohoku-Oki earthquake, Geophys. Res. Lett., 38, L23307, https://doi.org/10.1029/2011GL049795, 2011.

Molnar, P., and Lyon-Caen, H.: Some simple physical aspects of the support, structure, and evolution of mountain belts, in: Processes in continental lithospheric deformation, edited by: Clark Jr, S. P., Burchfiel, B. C., and Suppe, J., Geological Society of America, Boulder, CO, 179–208, 1998.

Moore, D. E., and Lockner, D. A.: Crystallographic control of the frictional behavior of dry and water-saturated sheet structure minerals, J. Geophys. Res., 109, B03401, doi:10.1029/2003JB002582, 2004.

Moreno, M., Haberland, C., Oncken, O., Rietbrock, A., Angiboust, S., and Heidbach, O.: Locking of the Chile subduction zone controlled by fluid pressure before the 2010 earthquake, Nat. Geosci., 7, 292–296, https://doi.org/10.1038/ngeo2102, 2014.

Moreno, M., Melnick, D., Rosenau, M., Baez, J., Klotz, J., Oncken, O., Tassara, A., Chen, J., Bataille, K., Bevis, M., Socquet, A., Bolte, J., Vigny, C., Brooks, B., Ryder, I., rund, V., Smalley, B., and Carrizo, D.: Toward understanding tectonic control on the Mw 8.8 2010 Maule Chile earthquake. Earth Planet. Sci. Lett., 321, 152–165. https://doi.org/10.1016/j.epsl.2012.01.006, 2012.

Nakamura, W., Uchida, N., and Matsuzawa, T.: Spatial distribution of the faulting types of small earthquakes around the 2011 Tohoku-oki earthquake: A comprehensive search using template events. J. Geophys. Res., 121, 2591– 2607, https://doi.org/10.1002/2015JB012584, 2016.

955   Oncken, O., Angiboust, S., and Dresen, G.: Slow slip in subduction zones: Reconciling deformation fabrics with instrumental observations and laboratory results, Geosphere, 18, 104– 129, https://doi.org/10.1130/GES02382.1, 2021.

Oppenheimer, D. H., Reasenberg, P. A., and Simpson R. W.: Fault plane solutions for the 1984 Morgan Hill, California, earthquake sequence: Evidence for the state of stress on the Calaveras fault, J. Geophys. Res., 93, 9007–9026, 1988.

Pace, B., Bocchini, G. M., and Boncio, P.: Do static stress changes of a moderate-magnitude earthquake significantly modify the regional seismic hazard? Hints from the L'Aquila 2009 normal-faulting earthquake (Mw 6.3, central Italy), Terra Nova,

960   26, 430-439, https://doi.org/10.1111/ter.12117, 2014.

Papazafeiropoulos, G., Muñiz-Calvente, M., and Martínez-Pañeda, E.: Abaqus2Matlab: a suitable tool for finite element post-processing, Adv. Eng. Softw., 105, 9–16, https://doi.org/10.1016/j.advengsoft.2017.01.006, 2017.

Peikert, J., Hampel, A., and Bagge, M.: Three-dimensional finite-element modeling of Coulomb stress changes on normal and thrust faults caused by pore fluid pressure changes and postseismic viscoelastic relaxation, Geosphere, 20, 105–128,

965   https://doi.org/10.1130/GES02672.1, 2024.

Peña, C., Metzger, S., Heidbach, O., Bedford, J., Bookhagen, B., Moreno, M., Oncken, O, and Cotton, F.: Role of poroelasticity during the early postseismic deformation of the 2010 Maule megathrust earthquake, Geophys. Res. Lett., 49, e2022GL098144, https://doi.org/10.1029/2022GL098144, 2022.

Qiu, Q., and Chan, C.-H.: Coulomb stress perturbation after great earthquakes in the Sumatran subduction zone: Potential

970   impacts in the surrounding region, J. Asian Earth Sci., 180, 103869, https://doi.org/10.1016/j.jseaes.2019.103869, 2019.

Ryder, I, Rietbrock, A., Kelson, K., Bürgmann, R., Floyd, M., Socquet, A., Vigny, C., and Carrizo, D.: Large extensional aftershocks in the continental forearc triggered by the 2010 Maule earthquake, Chile, Geophys. J. Int., 188, 879-890, https://doi.org/10.1111/j.1365-246X.2011.05321.x, 2012.

Saltogianni, V., Mouslopoulou, V., Dielforder, A., Bocchini, G. M., Bedford, J., and Oncken, O.: Slow slip triggers the 2018

975   M_w 6.9 Zakynthos earthquake within the weakly locked Hellenic subduction system, Greece, Geochem., Geophys., Geoys., 22, e2021GC010090, https://doi.org/10.1029/2021GC010090, 2021.

Sato, M., Ishikawa, T., Ujihara, N., Yoshida, S., Fujita, M., Mochizuki, M., and Asada, A.: Displacement above the hypocenter of the 2011 Tohoku-Oki earthquake, Science, 332, 1395, https://doi.org/10.1126/science.1207401, 2011.

Scholz, C. H.: Earthquakes and friction laws, Nature, 391, 37–42, 1998.

980   Schwanghart, W., & Scherler, D.: TopoToolbox 2—MATLAB-based software for topographic analysis and modeling in Earth surface sciences, Earth Surf. Dyn., 2, 1–7. https://doi.org/10.5194/esurf-2-1-2014, 2014.

Segou, M., and Parsons, T.: A new technique to calculate earthquake stress transfer and to probe the physics of aftershocks, Bull. Seismol. Soc. Am., 110, 863-873, https://doi.org/10.1785/0120190033, 2020.

Şen, A. T:, Cesca, S., Lange, D., Dahm, T., Tilmann, F., and Heimann, S.: Systematic changes of earthquake rupture with depth: a case study from the 2010 M_w 8.8 Maule, Chile, Earthquake aftershock sequence, Bull. Seismol. Soc. Am., 105, 2468-2479, https://doi.org/10.1785/0120140123, 2015.

Seno, T.: Determination of the pore fluid pressure ratio at seismogenic megathrusts in subduction zones: Implications for strength asperities and Andean-type mountain building, J. Geophys. Res., 114, B05405, https://doi.org/10.1029/2008JB005889, 2009.

Sibson, R. H.: Brittle failure mode plots for compressional and extensional tectonic regimes, J. Struct. Geol., 20, 655–660, https://doi.org/10.1016/0191-8141(85)90150-6, 1998.

Stein, R.: The role of stress transfer in earthquake occurrence, Nature, 402, 605–609, https://doi.org/10.1038/45144, 1999.

Stressler, B. J., and Barnhart, W. D.: An investigation of the accuracy of coulomb stress changes inferred from geodetic observations following subduction zone earthquakes, J. Geophys. Res., 122, 7467–7484, https://doi.org/10.1002/2017JB014461, 2017.

Sun, T., Wang, K., Fujiwara, T., Kodaira, S., and He, J.: Large fault slip peaking at trench in the 2011 Tohoku-Oki earthquake, Nature Communications, 8, https://doi.org/10.1038/ncomms14044, 2017.

Sun, T., Wang, K., Iinuma, T., Hino, R., He, J., Fujimoto, H., Kido, M., Osada, Y., Miura, S., Ohta, Y., and Hu, Y.: Prevalence of viscoelastic relaxation after the 2011 Tohoku-oki earthquake, Nature, 514, 84–87, https://doi.org/10.1038/nature13778, 2014.

Terakawa, T., Hashimoto, C., and Matsu'ura, M.: Changes in seismic activity following the 2011 Tohoku-oki earthquake: Effects of pore fluid pressure, Earth Planet. Sci. Lett., 365, 17–24, https://doi.org/10.1016/j.epsl.2013.01.017, 2013.

Tesei, T., Collettini, C., Carpenter, B. M., Viti, C., and Marone, C.: Frictional strength and healing behavior of phyllosilicate-rich faults, J. Geophys. Res., 117, B09402, https://doi.org/10.1029/2012JB009204, 2012.

The MathWorks Inc.: MATLAB version: 9.13.0 (R2022b), Natick, Massachusetts: The MathWorks Inc. https://www.mathworks.com, 2022.

Toda, S., Lin, J., and Stein, R.: Using the 2011 M_w 9.0 off the Pacific coast of Tohoku Earthquake to test the Coulomb stress triggering hypothesis and to calculate faults brought closer to failure, Earth Planets Space, 63, 725–7300. https://doi.org/10.5047/eps.2011.05.010, 2011a.

Toda, S., Stein, R. S., & Lin, J.: Widespread seismicity excitation throughout central Japan following the 2011 M=9.0 Tohoku earthquake and its interpretation by Coulomb stress transfer, Geophys. Res. Lett., 38, L00G03, https://doi.org/10.1029/2011GL047834, 2011b.

Tsuji, T., Kamei, R., and Pratt, R. G.: Pore pressure distribution of a mega-splay fault system in the Nankai subduction zone: Insight into up-dip extent of the seismogenic zone, Earth Planet. Sci. Lett., 396, 165-178, http://dx.doi.org/10.1016/j.epsl.2014.04.011, 2014.

Yoshida, K., Hasegawa, A., and Okada, T.: Spatially heterogeneous stress field in the source area of the 2011 M_w 6.6 Fukushima-Hamadori earthquake, NE Japan, probably caused by static stress change. Geophys. J. Int., 201, 1062–1071, https://doi.org/10.1093/gji/ggv068, 2015.

Yoshida, K., Hasegawa, A., Okada, T., Iinuma, T., Ito, Y., and Asano, Y., Stress before and after the 2011 great Tohoku-oki earthquake and induced earthquakes in inland areas of eastern Japan, Geophys. Res. Lett., 39, L03302, https://doi.org/10.1029/2011GL049729, 2012.

Yoshida, K., Saito, T., Urata, Y., Asano, Y., and Hasegawa, A.: Temporal changes in stress drop, frictional strength, and earthquake size distribution in the 2011 Yamagata-Fukushima, NE Japan, earthquake swarm, caused by fluid migration, J. Geophys. Res., 122, 10,379–10,397, https://doi.org/10.1002/2017JB014334, 2017.

van den Beukel, J., and Wortel, R.: Temperatures and shear stresses in the upper part of a subduction zone, Geophys. Res. Lett., 14, 1057–1060. https://doi.org/10.1029/GL014i010p01057, 1987.

van den Beukel, J., & Wortel, R.: Thermo-mechanical modelling of arc-trench regions. *Tectonophysics*, 154, 177–193, https://doi.org/10.1016/0040-1951(88)90101-1, 1988.

Wada, I., and Wang, K.: Common depth of slab-mantle decoupling: Reconciling diversity and uniformity of subduction zones, Geochem., Geophys., Geosys., 10, Q10009, https://doi.org/10.1029/2009GC002570, 2009.

Wang, K., Brown, L., Hu, Y., Yoshida, K., He, J., and Sun, T.: Stable forearc stressed by a weak megathrust: Mechanical and geodynamic implications of stress changes caused by the M = 9 Tohoku-Oki earthquake, J. Geophys. Res., 124, 6179–6194. https://doi.org/10.1029/2018JB017043, 2019.

Wang, K., and He, J.: Mechanics of low stress forearcs: Nankai and Cascadia, J. Geophys. Res., 104, 15191–15205. https://doi.org/10.1029/1999JB900103, 1999.

Wang, K., and Hu, Y.: Accretionary prisms in subduction earthquake cycles: The theory of dynamic Coulomb wedge, J. Geophys. Res., 111, B06410, https://doi.org/ 10.1029/2005JB004094, 2006.

Wang, K., Huang, T., Tilmann, F., Peacock, S. M., and Lange, D.: Role of serpentinized mantle wedge in affecting megathrust seismogenic behavior in the area of the 2010 M= 8.8 Maule earthquake, Geophys. Res. Lett., 47, e2020GL090482, https://doi.org/10.1029/2020GL090482, 2020.

Wei, S., Graves, R., Helmberger, D., Avouac, J., and Jiang, J.: Sources of shaking and flooding during the Tohoku-oki earthquake: A mixture of rupture styles, Earth Planet. Sci. Lett., 333–334, 91–100., 2012

Wessel, P., Luis, J. F., Uieda, L., Scharroo, R., Wobbe, F., Smith, W. H. F., and Tian, D.: The Generic Mapping Tools Version 6, Geochem., Geophys., Geosys., 20), 5556–5564, https://doi.org/10.1029/2019GC008515, 2019.

Wiemer, S., and Katsumata, K.: Spatial variability of seismicity parameters in aftershock zones. J. Geophys. Res., 104, 13135–13151, https://doi.org/10.1029/1999JB900032, 1999.

Wimpenny, S., Forrest, N., and Copley, A.: Time-dependent decrease in fault strength in the 2011–2016 Ibaraki–Fukushima earthquake sequence. Geophys. J. Int., 232, 788–809. https://doi.org/10.1093/gji/ggac368, 2023.

Yang, Y. R., Johnson, K. M., and Chuang, R. Y.: Inversion for absolute deviatoric crustal stress using focal mechanisms and coseismic stress changes: The 2011 M9 Tohoku-oki, Japan, earthquake, J. Geophys. Res., 118, 5516–5529, https://doi.org/10.1002/jgrb.50389, 2013.

Zhao, W. L., Davis, D. M., Dahlen, F. A., and Suppe, J.: Origin of convex accretionary wedges: Evidence from Barbados, J. Geophys. Res., 91, 10,246–10,258, 1986.

1050